Assessment of Several Artificial Dissipation Models in 2D and 3D

Edisson S. G. Maciel and Omar Seye

***Abstract*—**In this paper, the Euler equations in conservative and integral forms are applied to the solution of the supersonic flow along a compression corner. Five artificial dissipation models are tested, aiming to identify the main vantages and disadvantages of each one. Three isotropic models based on the works of Azevedo, Mavriplis, and MacCormack and Baldwin are implemented. On the other hand, two anisotropic models based on the work of Turkel and Vatsa are studied. The isotropic models are scalar ones, whereas the anisotropic models are scalar and matrix ones. Such studies are performed on a finite volume and structured contexts, in two- and three-dimensional spaces. The algorithms to perform the numerical experiments are the MacCormack, second order, MacCormack, fourth order, and Jameson and Mavriplis, second order, in two-dimensions. In three-dimensions, one studies the MacCormack, second order, and the Jameson and Mavriplis, second order. All schemes are predictor-corrector or symmetrical ones. Convergence is accelerated to the steady state by a spatially variable time step procedure, which has provided excellent results as reported by Maciel. Good results are obtained by all models, especially for the matrix model, and are reported in this paper.

***Keywords*—**Artificial dissipation models, Anisotropic scalar and matrix models, Euler equations, Isotropic scalar models, Jameson and Mavriplis scheme, MacCormack scheme.

I. Introduction

ARTIFICIAL dissipation is either explicitly added or naturally occurring in Computational Fluid Dynamic algorithms to provided convergence stability and suppress undesirable flow field oscillations. Solution accuracy depends on the proper amount of dissipation being added where required and not added where not required. For example, the numerical modeling of shock waves can require large levels of carefully constructed dissipation to prevent pre- and post-shock oscillations. Care also must be taken in regions of viscous dominated flow to prevent artificial dissipation from dominating real viscosity and destroying prediction accuracy. Unfortunately, many applications have become so complicated that it is nearly impossible to determine if the proper amount of artificial dissipation is being introduced into each area of the flow field. Today, studies of fundamental flow fields are still required to fully understand the effects of numerical dissipation on solutions accuracy.

In a detailed study of the grid requirements for viscous airfoil computations, [1] showed that numerical errors in drag can be high even on relatively fine grids. This represents an important impediment to the development of efficient flow solvers, as the grid requirements for accurate drag prediction are excessive, especially for three-dimensional computations. Several avenues are being explored to reduce numerical errors, such as solution-adaptive gridding, and higher-order discretizations. One area in which improvements are possible is in the method by which dissipation is included in the spatial discretization.

Several researchers have shown that the scalar artificial dissipation model commonly used with centered difference schemes can be a major source of numerical error, especially in laminar boundary layers and in drag prediction. Examples are given in [2-7]. This problem is reduced with upwind schemes and matrix dissipation. However, the scalar dissipation model is inexpensive and easy to implement. Consequently, some researchers have proposed scalings for the scalar dissipation model in an attempt to reduce numerical errors. These include scalings based on local Mach number and vorticity. However, these parameters are functions of the flow field only and do not account for the grid density. Since the amount of artificial dissipation needed is clearly dependent on the grid resolution, these scalings are neither general nor robust.

In this paper, the Euler equations in conservative and integral forms are applied to the solution of the supersonic flow along a compression corner. Five artificial dissipation models are tested, aiming to identify the main vantages and disadvantages of each one. Three isotropic models based on the works of [8], [9], and [10] are implemented. On the other hand, two anisotropic models based on the work of [3] are studied. The isotropic models are scalar ones, whereas the anisotropic models are scalar and matrix ones. Such studies are performed on a finite volume and structured contexts, in two- and three-dimensional spaces. The algorithms to perform the numerical experiments are the [11], second order, the [12], fourth order, and the [13], second order, in two-dimensions. In three-dimensions, one studies the [11], second order, and the [13], second order. All schemes are predictor-corrector or

Edisson S. G. Maciel works as a post-doctorate researcher at ITA (Aeronautical Technological Institute) – Praça Marechal do Ar Eduardo Gomes, 50 – Vila das Acácias – São José dos Campos – SP – Brazil – 12228-900 (corresponding author, phone number: +55 012 99165-3565; e-mail: edisavio@edissonsavio.eng.br).

Omar Seye teaches at the Dederal University of Great Dourados, Rodovia Dourados – Itahum, km 12 – Caixa Postal 364 – Dourados, MS, Brazil – 79804-970 (second author, phone number: +55 067 3410-2173; e-mail: omarseye@ufgd.edu.br)

symmetrical ones. Convergence is accelerated to the steady state by a spatially variable time step procedure, which has provided excellent results as reported by [14-15]. Good results are obtained by all models, especially for the matrix model, and are reported in this paper.

II. EULER EQUATIONS IN 2D

The fluid movement is described by the Euler equations, which express the conservation of mass, of linear momentum and of energy to an inviscid, heat non-conductor and compressible mean, in the absence of external forces. In the integral and conservative forms, these equations can be represented by:

$$\frac{\partial}{\partial t}\int_V Q dV + \int_S \left(E_e n_x + F_e n_y\right) dS = 0, \qquad (1)$$

where Q is written to a Cartesian system, V is a cell volume, n_x and n_y are the components of the normal unity vector to the flux face, S is the surface area and E_e and F_e represent the components of the convective flux vector. Q, E_e and F_e are represented by:

$$Q = \begin{Bmatrix} \rho \\ \rho u \\ \rho v \\ e \end{Bmatrix}, \; E_e = \begin{Bmatrix} \rho u \\ \rho u^2 + p \\ \rho uv \\ (e+p)u \end{Bmatrix}, \; F_e = \begin{Bmatrix} \rho v \\ \rho uv \\ \rho v^2 + p \\ (e+p)v \end{Bmatrix}, \qquad (2)$$

being ρ the fluid density; u and v the Cartesian components of the velocity vector in the x and y directions, respectively; e the total energy per unity volume of the fluid mean; and p the static pressure of the fluid mean.

The Euler equations were nondimensionalized in relation to the freestream density, ρ_∞, and in relation to the freestream speed of sound, a_∞. The matrix system of the Euler equations is closed with the state equation of a perfect gas:

$$p = (\gamma - 1)\left[e - 0.5\rho(u^2 + v^2)\right] \qquad (3)$$

and γ being the ratio of specific heats. The total enthalpy is determined by $H = (e+p)/\rho$.

III. EULER EQUATIONS IN 3D

The fluid movement is described by the Euler equations, which express the conservation of mass, of momentum and of energy to an inviscid, heat non-conductor and compressible mean, in the absence of external forces. In the integral and conservative forms, these equations can be represented by:

$$\partial/\partial t \int_V Q dV + \int_S \left[E_e n_x + F_e n_y + G_e n_z\right] dS = 0, \quad (4)$$

where n_x, n_y and n_z are components of the normal unity vector to the flux face; and Ee, Fe and Ge are the components of the convective flux vector. The vectors Q, Ee, Fe and Ge are represented by:

$$Q = \begin{Bmatrix} \rho \\ \rho u \\ \rho v \\ \rho w \\ e \end{Bmatrix}, \; E_e = \begin{Bmatrix} \rho u \\ \rho u^2 + p \\ \rho uv \\ \rho uw \\ (e+p)u \end{Bmatrix}, \; F_e = \begin{Bmatrix} \rho v \\ \rho uv \\ \rho v^2 + p \\ \rho vw \\ (e+p)v \end{Bmatrix};$$

$$G_e = \begin{Bmatrix} \rho w \\ \rho uw \\ \rho vw \\ \rho w^2 + p \\ (e+p)w \end{Bmatrix}, \qquad (5)$$

where u, v and w are the Cartesian components of the velocity vector in the x, y and z directions, respectively. The matrix system of Euler equations is closed with the state equation of a perfect gas, similar to Eq. (3).

IV. ARTIFICIAL DISSIPATION MODELS IN 2D

The artificial dissipation models implemented in the [11-13] algorithms are based on the works of [3, 8-10] and have the following structure:

$$D(Q_{i,j}) = d^{(2)}(Q_{i,j}) - d^{(4)}(Q_{i,j}), \qquad (6)$$

with:

$$\begin{aligned} d^{(2)} = {} & 0.5\varepsilon^{(2)}_{i,j-1/2}\left(A_{i,j} + A_{i,j-1}\right)\left(Q_{i,j-1} - Q_{i,j}\right) + \\ & 0.5\varepsilon^{(2)}_{i+1/2,j}\left(A_{i,j} + A_{i+1,j}\right)\left(Q_{i+1,j} - Q_{i,j}\right) + \\ & 0.5\varepsilon^{(2)}_{i,j+1/2}\left(A_{i,j} + A_{i,j+1}\right)\left(Q_{i,j+1} - Q_{i,j}\right) + \\ & 0.5\varepsilon^{(2)}_{i-1/2,j}\left(A_{i,j} + A_{i-1,j}\right)\left(Q_{i-1,j} - Q_{i,j}\right), \end{aligned} \qquad (7)$$

named the undivided Laplacian operator, responsible by the numerical stability in presence of shock waves; and

$$\begin{aligned} d^{(4)} = {} & 0.5\varepsilon^{(4)}_{i,j-1/2}\left(A_{i,j} + A_{i,j-1}\right)\left(\nabla^2 Q_{i,j-1} - \nabla^2 Q_{i,j}\right) + \\ & 0.5\varepsilon^{(4)}_{i+1/2,j}\left(A_{i,j} + A_{i+1,j}\right)\left(\nabla^2 Q_{i+1,j} - \nabla^2 Q_{i,j}\right) + \\ & 0.5\varepsilon^{(4)}_{i,j+1/2}\left(A_{i,j} + A_{i,j+1}\right)\left(\nabla^2 Q_{i,j+1} - \nabla^2 Q_{i,j}\right) + \\ & 0.5\varepsilon^{(4)}_{i-1/2,j}\left(A_{i,j} + A_{i-1,j}\right)\left(\nabla^2 Q_{i-1,j} - \nabla^2 Q_{i,j}\right), \end{aligned} \quad (8)$$

named the bi-harmonic operator, responsible by the background stability (odd-even instabilities, for instance). In this last term,

$$\nabla^2 Q_{i,j} = \left(Q_{i,j-1} - Q_{i,j}\right) + \left(Q_{i+1,j} - Q_{i,j}\right) + \left(Q_{i,j+1} - Q_{i,j}\right) + \left(Q_{i-1,j} - Q_{i,j}\right). \quad (9)$$

In the d(4) operator, $\nabla^2 Q_{i,j}$ is extrapolated from your neighbour cell every time that such one represent an especial boundary layer cell, recognized in the CFD literature as "ghost" cell. The ε terms are defined, for instance, as:

$$\varepsilon^{(2)}_{i,j-1/2} = K^{(2)} MAX\left(\nu_{i,j}, \nu_{i,j-1}\right) \text{ and } \varepsilon^{(4)}_{i,j-1/2} = MAX\left[0, \left(K^{(4)} - \varepsilon^{(2)}_{i,j-1/2}\right)\right], \quad (10)$$

in which:

$$\nu_{i,j} = \left(\left|p_{i,j-1} - p_{i,j}\right| + \left|p_{i+1,j} - p_{i,j}\right| + \left|p_{i,j+1} - p_{i,j}\right| + \left|p_{i-1,j} - p_{i,j}\right|\right) \Big/ \left(p_{i,j-1} + p_{i+1,j} + p_{i,j+1} + p_{i-1,j} + 4p_{i,j}\right). \quad (11)$$

represents a pressure sensor employed to identify regions of high gradients. Each time that a neighbour cell represent a ghost cell, it is assumed that, for instance, $\nu_{ghost} = \nu_{i,j}$. The $A_{i,j}$ terms define the particular artificial dissipation operator. Five models were studied in this work:

(a) Artificial dissipation operator of [8] / Scalar, non-linear, and isotropic model:

In this case, the $A_{i,j}$ terms represent the sum of the contributions of the maximum normal eigenvalue associated to the flux interface of the Euler equations, integrated along each cell face. Based on [8] work, these terms are defined as:

$$A_{i,j} = \left|u_{int}S_x + v_{int}S_y\right|_{i,j-1/2} + a_{int}\left(S_x^2 + S_y^2\right)^{0.5}_{i,j-1/2} + \left|u_{int}S_x + v_{int}S_y\right|_{i+1/2,j} + a_{int}\left(S_x^2 + S_y^2\right)^{0.5}_{i+1/2,j} + \left|u_{int}S_x + v_{int}S_y\right|_{i,j+1/2} + a_{int}\left(S_x^2 + S_y^2\right)^{0.5}_{i,j+1/2} + \left|u_{int}S_x + v_{int}S_y\right|_{i-1/2,j} + a_{int}\left(S_x^2 + S_y^2\right)^{0.5}_{i-1/2,j}, \quad (12)$$

where "a" represents the sound speed and the interface properties are evaluated by arithmetical average. The $K^{(2)}$ and $K^{(4)}$ constants have typical values of 1/4 and 3/256, respectively.

(b) Artificial dissipation model of [9] / Scalar, non-linear, and isotropic model:

In the model proposed by [9], the $A_{i,j}$ weighting term is defined as follows:

$$A_{i,j} = V_{i,j} / \Delta t_{i,j}, \quad (13)$$

which represents a scaling fator, according to the structured mesh context, with the desired behavior to the artificial dissipation term: (a) bigger volumes result in bigger values of dissipation term; (b) smaller Δt's result in bigger values of the scaling term. The other parameters maintain unaltered. The $K^{(2)}$ and $K^{(4)}$ constants have typical values of 1/4 and 3/256, respectively.

(c) Artificial dissipation model of [10] / Scalar, non-linear, and isotropic model:

In this case, the $A_{i,j}$ terms are vectors and represent the contributions of the maximum normal eigenvalue associated to the flux interface of the Euler equations, integrated long each cell face. Each normal eigenvalue is associated with a conservation equation. Only the non-linear dissipation is considered. Based on [10] work, these terms are defined as:

$$A^{(1)}_{i,j} = \left(\left|un_x + vn_y\right| + a\right)_{i,j-1/2} S_{i,j-1/2};$$
$$A^{(2)}_{i,j} = \left(\left|un_x + vn_y\right| + a\right)_{i+1/2,j} S_{i+1/2,j};$$
$$A^{(3)}_{i,j} = \left(\left|un_x + vn_y\right| + a\right)_{i,j+1/2} S_{i,j+1/2};$$
$$A^{(4)}_{i,j} = \left(\left|un_x + vn_y\right| + a\right)_{i-1/2,j} S_{i-1/2,j}, \quad (14)$$

with the ε terms defined, as for example:

$$\varepsilon^{(2)}_{i,j-1/2} = K^{(2)} \frac{\nu_{i,j} + \nu_{i,j-1}}{2}. \quad (15)$$

The $K^{(2)}$ constant has a typical value of 1/2. In the present work, the [10] dissipation model is added in both predictor and corrector steps of the [11,12] schemes.

(d) Artificial dissipation model of [3] / Scalar, non-linear, and anisotropic model:

The aforementioned artificial dissipation models present the characteristic of being isotropic. In words, the dissipation introduced artificially in a given coordinate direction to stabilize the scheme weights equally the phenomena originated from all directions, having not a more significant weighting from the particular direction under study. The dissipation is clearly isotropic. The scalar, non-linear and anisotropic artificial dissipation model of [3] aims to provide a numerical attenuation that considers with bigger weight the propagation information effects associated to the characteristic maximum eigenvalue from the coordinate direction under study. Basically, such artificial dissipation model differs from the non-linear, isotropic models of [8-10] only in the determination of the weighting term of the dissipation operator.

$$A_\xi = \overline{\lambda}_{\xi_{i+1/2,j}}\left[1+\left(\overline{\lambda}_\eta \big/ \overline{\lambda}_\xi\right)^{0.5}_{i+1/2,j}\right] \text{ and}$$

$$\overline{\lambda}_{\xi_{i+1/2,j}} = \left(\left|un_x + vn_y\right| + a\right)_{i+1/2,j} S_{i+1/2,j}; \qquad (16)$$

$$A_\eta = \overline{\lambda}_{\eta_{i,j+1/2}}\left[1+\left(\overline{\lambda}_\xi \big/ \overline{\lambda}_\eta\right)^{0.5}_{i,j+1/2}\right] \text{ and}$$

$$\overline{\lambda}_{\eta_{i,j+1/2}} = \left(\left|un_x + vn_y\right| + a\right)_{i,j+1/2} S_{i,j+1/2}. \qquad (17)$$

To this artificial dissipation model, the recommended values of $K^{(2)}$ e $K^{(4)}$ by [3] are 1/2 and 1/64, respectively.

(e) Artificial dissipation model of [3] / Matrix, non-linear, and anisotropic model:

The anisotropic, non-linear and matrix artificial dissipation model of [3] considers different quantities of numerical attenuation applied to each conservation equation in its discrete form aiming to provide smaller artificial dissipation, as preconized by the authors. In this case, the weighting term or the scalar scaling is replaced by a matrix term defined by the "modulus" of the Jacobian flux matrices. Mathematically, it can be represented by:

$$A_\xi = \left|\hat{A}\right|_{i+1/2,j} = \left(R_\xi \left|\lambda_\xi\right| R_\xi^{-1}\right)_{i+1/2,j}; \qquad (18)$$

$$A_\eta = \left|\hat{B}\right|_{i,j+1/2} = \left(R_\eta \left|\lambda_\eta\right| R_\eta^{-1}\right)_{i,j+1/2}. \qquad (19)$$

The right and left eigenvectors of the inviscid Jacobian matrix, which form the R and R-1 matrices, are given by:

$$R = \begin{bmatrix} 1 & 1 & 0 \\ u_{int} - h_x' a_{int} & u_{int} & -h_y' \\ v_{int} - h_y' a_{int} & v_{int} & h_x' \\ H_{int} - h_x' u_{int} a_{int} - h_y' v_{int} a_{int} & 0.5\left(u_{int}^2 + v_{int}^2\right) & h_x' v_{int} - h_y' u_{int} \end{bmatrix}$$

$$\begin{bmatrix} 1 \\ u_{int} + h_x' a_{int} \\ v_{int} + h_y' a_{int} \\ H_{int} + h_x' u_{int} a_{int} + h_y' v_{int} a_{int} \end{bmatrix}; \qquad (20)$$

$$R^{-1} = \begin{bmatrix} \frac{1}{2}\left[\frac{\gamma-1}{a_{int}^2}\frac{\left(u_{int}^2+v_{int}^2\right)}{2} + \frac{1}{a_{int}}\left(u_{int}h_x' + v_{int}h_y'\right)\right] & \frac{1}{2}\left(-\frac{\gamma-1}{a_{int}^2}u_{int} - \frac{h_x'}{a_{int}}\right) & \frac{1}{2}\left(-\frac{\gamma-1}{a_{int}^2}v_{int} - \frac{h_y'}{a_{int}}\right) & \frac{\gamma-1}{2a_{int}^2} \\ 1 - \frac{\gamma-1}{a_{int}^2}\frac{\left(u_{int}^2+v_{int}^2\right)}{2} & \frac{\gamma-1}{a_{int}^2}u_{int} & \frac{\gamma-1}{a_{int}^2}v_{int} & -\frac{\gamma-1}{a_{int}^2} \\ -\left(h_x'v_{int} - h_y'u_{int}\right) & -h_y' & h_x' & 0 \\ \frac{1}{2}\left[\frac{\gamma-1}{a_{int}^2}\frac{\left(u_{int}^2+v_{int}^2\right)}{2} - \frac{1}{a_{int}}\left(u_{int}h_x' + v_{int}h_y'\right)\right] & \frac{1}{2}\left(-\frac{\gamma-1}{a_{int}^2}u_{int} + \frac{h_x'}{a_{int}}\right) & \frac{1}{2}\left(-\frac{\gamma-1}{a_{int}^2}v_{int} + \frac{h_y'}{a_{int}}\right) & \frac{\gamma-1}{2a_{int}^2} \end{bmatrix}, \qquad (21)$$

where h_x' and h_y' are normalized metric terms. In practice, the modulus of the inviscid Jacobian matrix eigenvalues can be equal to zero close to stagnation points or sonic points, resulting in dissipation absence. To avoid such problem, these parameters are limited by the expressions below:

$$\left|\lambda_\xi\right|_{i+1/2,j} = \text{MAX}\left(\left|\lambda_\xi\right|,\ \varphi\overline{\lambda}_\xi\right); \qquad (22)$$

$$\left|\lambda_\eta\right|_{i,j+1/2} = \text{MAX}\left(\left|\lambda_\eta\right|,\ \varphi\overline{\lambda}_\eta\right), \qquad (23)$$

in which the value $\varphi = 0.5$ was employed in this work.

V. ARTIFICIAL DISSIPATION MODELS IN 3D

The artificial dissipation models implemented in the [11,13] algorithms are based on the works of [3, 8-10] and have the following structure:

$$D\left(Q_{i,j,k}\right) = d^{(2)}\left(Q_{i,j,k}\right) - d^{(4)}\left(Q_{i,j,k}\right), \qquad (24)$$

with:

$$\begin{aligned} d^{(2)} = {} & 0.5\varepsilon^{(2)}_{i,j-1/2,k}\left(A_{i,j,k} + A_{i,j-1,k}\right)\left(Q_{i,j-1,k} - Q_{i,j,k}\right) + \\ & 0.5\varepsilon^{(2)}_{i+1/2,j,k}\left(A_{i,j,k} + A_{i+1,j,k}\right)\left(Q_{i+1,j,k} - Q_{i,j,k}\right) + \\ & 0.5\varepsilon^{(2)}_{i,j+1/2,k}\left(A_{i,j,k} + A_{i,j+1,k}\right)\left(Q_{i,j+1,k} - Q_{i,j,k}\right) + \\ & 0.5\varepsilon^{(2)}_{i-1/2,j,k}\left(A_{i,j,k} + A_{i-1,j,k}\right)\left(Q_{i-1,j,k} - Q_{i,j,k}\right) + \\ & 0.5\varepsilon^{(2)}_{i,j,k-1/2}\left(A_{i,j,k} + A_{i,j,k-1}\right)\left(Q_{i,j,k-1} - Q_{i,j,k}\right) + \\ & 0.5\varepsilon^{(2)}_{i,j,k+1/2}\left(A_{i,j,k} + A_{i,j,k+1}\right)\left(Q_{i,j,k+1} - Q_{i,j,k}\right), \end{aligned} \qquad (25)$$

named the undivided Laplacian operator, responsible by the numerical stability in presence of shock waves; and

$$\begin{aligned} d^{(4)} = {} & 0.5\varepsilon^{(4)}_{i,j-1/2,k}\left(A_{i,j,k} + A_{i,j-1,k}\right)\left(\nabla^2 Q_{i,j-1,k} - \nabla^2 Q_{i,j,k}\right) + \\ & 0.5\varepsilon^{(4)}_{i+1/2,j,k}\left(A_{i,j,k} + A_{i+1,j,k}\right)\left(\nabla^2 Q_{i+1,j,k} - \nabla^2 Q_{i,j,k}\right) + \\ & 0.5\varepsilon^{(4)}_{i,j+1/2,k}\left(A_{i,j,k} + A_{i,j+1,k}\right)\left(\nabla^2 Q_{i,j+1,k} - \nabla^2 Q_{i,j,k}\right) + \\ & 0.5\varepsilon^{(4)}_{i-1/2,j,k}\left(A_{i,j,k} + A_{i-1,j,k}\right)\left(\nabla^2 Q_{i-1,j,k} - \nabla^2 Q_{i,j,k}\right) + \\ & 0.5\varepsilon^{(4)}_{i,j,k-1/2}\left(A_{i,j,k} + A_{i,j,k-1}\right)\left(\nabla^2 Q_{i,j,k-1} - \nabla^2 Q_{i,j,k}\right) + \\ & 0.5\varepsilon^{(4)}_{i,j,k+1/2}\left(A_{i,j,k} + A_{i,j,k+1}\right)\left(\nabla^2 Q_{i,j,k+1} - \nabla^2 Q_{i,j,k}\right), \end{aligned} \quad (26)$$

named the bi-harmonic operator, responsible by the background stability (odd-even instabilities, for instance). In this last term,

$$\begin{aligned} \nabla^2 Q_{i,j,k} = {} & \left(Q_{i,j-1,k} - Q_{i,j,k}\right) + \left(Q_{i+1,j,k} - Q_{i,j,k}\right) + \\ & \left(Q_{i,j+1,k} - Q_{i,j,k}\right) + \left(Q_{i-1,j,k} - Q_{i,j,k}\right) + \\ & \left(Q_{i,j,k-1} - Q_{i,j,k}\right) + \left(Q_{i,j,k+1} - Q_{i,j,k}\right). \end{aligned} \quad (27)$$

In the $d^{(4)}$ operator, $\nabla^2 Q_{i,j,k}$ is extrapolated from your neighbour cell every time that such one represent an especial boundary layer cell, recognized in the CFD literature as "ghost" cell. The ε terms are defined, for instance, as:

$$\begin{aligned} \varepsilon^{(2)}_{i,j-1/2,k} &= K^{(2)} MAX\left(\nu_{i,j,k}, \nu_{i,j-1,k}\right) \text{ and} \\ \varepsilon^{(4)}_{i,j-1/2,k} &= MAX\left[0, \left(K^{(4)} - \varepsilon^{(2)}_{i,j-1/2,k}\right)\right], \end{aligned} \quad (28)$$

in which:

$$\begin{aligned} \nu_{i,j,k} = {} & \left(\left|p_{i,j-1,k} - p_{i,j,k}\right| + \left|p_{i+1,j,k} - p_{i,j,k}\right| + \left|p_{i,j+1,k} - p_{i,j,k}\right| + \right. \\ & \left. \left|p_{i-1,j,k} - p_{i,j,k}\right| + \left|p_{i,j,k-1} - p_{i,j,k}\right| + \left|p_{i,j,k+1} - p_{i,j,k}\right|\right) \Big/ \\ & \left(p_{i,j-1,k} + p_{i+1,j,k} + p_{i,j+1,k} + p_{i-1,j,k} + p_{i,j,k-1} + p_{i,j,k+1} + 6p_{i,j,k}\right), \end{aligned} \quad (29)$$

represents a pressure sensor employed to identify regions of high gradients. Each time that a neighbour cell represent a ghost cell, it is assumed that, for instance, $\nu_{ghost} = \nu_{i,j,k}$. The $A_{i,j,k}$ terms define the particular artificial dissipation operator. Five models were studied in this work:

(a) Artificial dissipation operator of [8] / Scalar, non-linear, and isotropic model:

As mentioned in the 2D dissipation models, the Ai,j,k terms represent the sum of the contributions of the maximum normal eigenvalue associated to the flux interface of the Euler equations, integrated along each cell face. Based on [8] work, these terms are defined as:

$$\begin{aligned} A_{i,j,k} = {} & \left|u_{int}S_x + v_{int}S_y + w_{int}S_z\right|_{i,j-1/2,k} + a_{int}\left(S_x^2 + S_y^2 + S_z^2\right)^{0.5}_{i,j-1/2,k} + \\ & \left|u_{int}S_x + v_{int}S_y + w_{int}S_z\right|_{i+1/2,j,k} + a_{int}\left(S_x^2 + S_y^2 + S_z^2\right)^{0.5}_{i+1/2,j,k} + \\ & \left|u_{int}S_x + v_{int}S_y + w_{int}S_z\right|_{i,j+1/2,k} + a_{int}\left(S_x^2 + S_y^2 + S_z^2\right)^{0.5}_{i,j+1/2,k} + \\ & \left|u_{int}S_x + v_{int}S_y + w_{int}S_z\right|_{i-1/2,j,k} + a_{int}\left(S_x^2 + S_y^2 + S_z^2\right)^{0.5}_{i-1/2,j,k} + \\ & \left|u_{int}S_x + v_{int}S_y + w_{int}S_z\right|_{i,j,k-1/2} + a_{int}\left(S_x^2 + S_y^2 + S_z^2\right)^{0.5}_{i,j,k-1/2} + \\ & \left|u_{int}S_x + v_{int}S_y + w_{int}S_z\right|_{i,j,k+1/2} + a_{int}\left(S_x^2 + S_y^2 + S_z^2\right)^{0.5}_{i,j,k+1/2}, \end{aligned} \quad (30)$$

where the interface variables are defined by arithmetical average.

(b) Artificial dissipation model of [9] / Scalar, non-linear, and isotropic model:

In this model, the $A_{i,j,k}$ weighting term is defined as follows:

$$A_{i,j,k} = V_{i,j,k} / \Delta t_{i,j,k}, \quad (31)$$

which represents a scaling fator, according to the structured mesh context, with the desired behavior to the artificial dissipation term.

(c) Artificial dissipation model of [10] / Scalar, non-linear, and isotropic model:

As seen in the two-dimensional case, the $A_{i,j,k}$ terms are vectors and represent the contributions of the maximum normal eigenvalue associated to the flux interface of the Euler equations, integrated long each cell face. Based on [10] work, these terms are defined as:

$$\begin{aligned} A^{(1)}_{i,j,k} &= \left(\left|un_x + vn_y + wn_z\right| + a\right)_{i,j-1/2,k} S_{i,j-1/2,k}; \\ A^{(2)}_{i,j,k} &= \left(\left|un_x + vn_y + wn_z\right| + a\right)_{i+1/2,j,k} S_{i+1/2,j,k}; \\ A^{(3)}_{i,j,k} &= \left(\left|un_x + vn_y + wn_z\right| + a\right)_{i,j+1/2,k} S_{i,j+1/2,k}; \\ A^{(4)}_{i,j,k} &= \left(\left|un_x + vn_y + wn_z\right| + a\right)_{i-1/2,j,k} S_{i-1/2,j,k}; \\ A^{(5)}_{i,j,k} &= \left(\left|un_x + vn_y + wn_z\right| + a\right)_{i,j,k-1/2} S_{i,j,k-1/2}; \\ A^{(6)}_{i,j,k} &= \left(\left|un_x + vn_y + wn_z\right| + a\right)_{i,j,k+1/2} S_{i,j,k+1/2}, \end{aligned} \quad (32)$$

with the ε terms defined, as for example:

$$\varepsilon^{(2)}_{i,j-1/2,k} = K^{(2)} \frac{\nu_{i,j,k} + \nu_{i,j-1,k}}{2}. \qquad (33)$$

(d) Artificial dissipation model of [3] / Scalar, non-linear, and anisotropic model:

The [3] scalar, non-linear and anisotropic model of [3] is defined in the last section and corresponds to the contribution of the normal eigenvalues to each cell face. The anisotropic property of this model is due to the different weights that are considered in its definition. The normal eigenvalues are the weighting terms.

$$A_\xi = \bar{\lambda}_{\xi_{i+1/2,j,k}} \left[1+\left(\bar{\lambda}_\eta / \bar{\lambda}_\xi\right)^{0.5}_{i+1/2,j,k}\right]\left[1+\left(\bar{\lambda}_\zeta / \bar{\lambda}_\xi\right)^{0.5}_{i+1/2,j,k}\right];$$

$$\bar{\lambda}_{\xi_{i+1/2,j,k}} = \left(\left|un_x + vn_y + wn_z\right| + a\right)_{i+1/2,j,k} S_{i+1/2,j,k}; \quad (34)$$

$$A_\eta = \bar{\lambda}_{\eta_{i,j+1/2,k}} \left[1+\left(\bar{\lambda}_\xi / \bar{\lambda}_\eta\right)^{0.5}_{i,j+1/2,k}\right]\left[1+\left(\bar{\lambda}_\zeta / \bar{\lambda}_\eta\right)^{0.5}_{i,j+1/2,k}\right];$$

$$\bar{\lambda}_{\eta_{i,j+1/2,k}} = \left(\left|un_x + vn_y + wn_z\right| + a\right)_{i,j+1/2,k} S_{i,j+1/2,k}; \quad (35)$$

$$A_\zeta = \bar{\lambda}_{\zeta_{i,j,k+1/2}} \left[1+\left(\bar{\lambda}_\xi / \bar{\lambda}_\zeta\right)^{0.5}_{i,j,k+1/2}\right]\left[1+\left(\bar{\lambda}_\eta / \bar{\lambda}_\zeta\right)^{0.5}_{i,j,k+1/2}\right];$$

$$\bar{\lambda}_{\zeta_{i,j,k+1/2}} = \left(\left|un_x + vn_y + wn_z\right| + a\right)_{i,j,k+1/2} S_{i,j,k+1/2}. \quad (36)$$

(e) Artificial dissipation model of [3] / Matrix, non-linear, and anisotropic model:

The anisotropic, non-linear and matrix artificial dissipation model of [3] considers different quantities of numerical attenuation applied to each conservation equation in its discrete form aiming to provide smaller artificial dissipation, as preconized by the authors. In this case, the weighting term or the scalar scaling is replaced by a matrix term defined by the "modulus" of the Jacobian flux matrices. Mathematically, it can be represented by:

$$A_\xi = \left|\hat{A}\right|_{i+1/2,j,k} = \left(R_\xi \left|\lambda_\xi\right| R_\xi^{-1}\right)_{i+1/2,j,k}; \qquad (37)$$

$$A_\eta = \left|\hat{B}\right|_{i,j+1/2,k} = \left(R_\eta \left|\lambda_\eta\right| R_\eta^{-1}\right)_{i,j+1/2,k}; \qquad (38)$$

$$A_\zeta = \left|\hat{C}\right|_{i,j,k+1/2} = \left(R_\zeta \left|\lambda_\zeta\right| R_\zeta^{-1}\right)_{i,j,k+1/2}. \qquad (39)$$

The right and left eigenvectors of the inviscid Jacobian matrix, which form the R and R^{-1} matrices, are given by:

$$[R] = \begin{bmatrix} 1 & 1 & 0 & 0 & 1 \\ u_l - h'_x a_l & u_l & h'_y & h'_z & u_l + h'_x a_l \\ v_l - h'_y a_l & v_l & h'_z & h'_x & v_l + h'_y a_l \\ w_l - h'_z a_l & w_l & h'_x & h'_y & w_l + h'_z a_l \\ H_l - h'_x u_l a_l - h'_y v_l a_l - h'_z w_l a_l & 0.5q^2 & h'_x w_l + h'_z v_l + h'_y u_l & h'_y w_l + h'_x v_l + h'_z u_l & H_l + h'_x u_l a_l + h'_y v_l a_l + h'_z w_l a_l \end{bmatrix}; \qquad (40)$$

$$[R^{-1}] = \begin{bmatrix} 0.5\left[\left(\gamma-1\right)/a_l^2\right)0.5q^2 + \phi/a_l\right] & -0.5\left[\left(\gamma-1\right)/a_l^2\right)u_l + h'_x/a_l\right] & -0.5\left[\left(\gamma-1\right)/a_l^2\right)v_l + h'_y/a_l\right] & -0.5\left[\left(\gamma-1\right)/a_l^2 w_l + h'_z/a_l\right] & 0.5\left(\gamma-1\right)/a_l^2\right] \\ 1-\left(\left(\gamma-1\right)/a_l^2\right)0.5q^2 & \left(\left(\gamma-1\right)/a_l^2\right)u_l & \left(\left(\gamma-1\right)/a_l^2\right)v_l & \left(\gamma-1\right)/a_l^2 w_l & -\left(\gamma-1\right)/a_l^2 \\ -\left(h'_y u_l + h'_z v_l + h'_x w_l\right) & h'_y & h'_z & h'_x & 0 \\ -\left(h'_z u_l + h'_x v_l + h'_y w_l\right) & h'_z & h'_x & h'_y & 0 \\ 0.5\left[\left(\gamma-1\right)/a_l^2\right)0.5q^2 - \phi/a_l\right] & 0.5\left[-\left(\left(\gamma-1\right)/a_l^2\right)u_l + h'_x/a_l\right] & 0.5\left[-\left(\left(\gamma-1\right)/a_l^2\right)v_l + h'_y/a_l\right] & 0.5\left[-\left(\gamma-1\right)/a_l^2 w_l + h'_z/a_l\right] & 0.5\left(\gamma-1\right)/a_l^2\right] \end{bmatrix}, \qquad (41)$$

where h'_x, h'_y and h'_z are normalized metric terms. In practice, the modulus of the inviscid Jacobian matrix eigenvalues can be equal to zero close to stagnation points or sonic points, resulting in dissipation absence. To avoid such problem, these parameters are limited by the expressions below:

$$\left|\lambda_\xi\right|_{i+1/2,j,k} = \mathrm{MAX}\left(\left|\lambda_\xi\right|, \varphi\bar{\lambda}_\xi\right); \qquad (42)$$

$$\left|\lambda_\eta\right|_{i,j+1/2,k} = \mathrm{MAX}\left(\left|\lambda_\eta\right|, \varphi\bar{\lambda}_\eta\right), \qquad (43)$$

$$\left|\lambda_\zeta\right|_{i,j,k+1/2} = \mathrm{MAX}\left(\left|\lambda_\zeta\right|, \varphi\bar{\lambda}_\zeta\right), \qquad (44)$$

in which the value $\varphi = 0.5$ was employed in this work.

VI. Algorithms in 2D

A. MacCormack, 2nd Order

Using finite volumes and applying the Green theorem to Equation (1), it is possible to write that:

$$\partial Q_{i,j}/\partial t = -1/V_{i,j}\int_S \left(\vec{F}\bullet\vec{n}\right)_{i,j} dS_{i,j}. \quad (45)$$

In the discretization of the surface integral, the Eq. (45) can be rewritten as:

$$dQ_{i,j}/dt = -1/V_{i,j}\left[\left(\vec{F}\bullet\vec{S}\right)_{i,j-1/2} + \left(\vec{F}\bullet\vec{S}\right)_{i+1/2,j} + \left(\vec{F}\bullet\vec{S}\right)_{i,j+1/2} + \left(\vec{F}\bullet\vec{S}\right)_{i-1/2,j}\right]. \quad (46)$$

Discretizing Equation (46) in time using the Euler explicit method, results in:

$$Q_{i,j}^{n+1} = Q_{i,j}^{n} - \Delta t_{i,j}/V_{i,j}\left[(F\cdot S)_{i,j-1/2} + (F\cdot S)_{i+1/2,j} + (F\cdot S)_{i,j+1/2} + (F\cdot S)_{i-1/2,j}\right]^n. \quad (47)$$

The time integration is now divided in two steps: one predictor and the other corrector. In the predictor step, the flux terms are calculated using the properties of the forward cell in relation to the flux interface. In the corrector step, the properties of the backward cell in relation to the flux interface are used. With this procedure, the scheme is second order accurate in space and time. Hence, the [11] algorithm, based on a finite volume formulation, is described as follows.
Predictor step:

$$\Delta Q_{i,j}^{n} = -\Delta t_{i,j}/V_{i,j}\left[\left(E_e\right)_{i,j}S_{x\,i,j-1/2} + \left(F_e\right)_{i,j}S_{y_{i,j-1/2}} + \left(E_e\right)_{i+1,j}S_{x\,i+1/2,j} + \left(F_e\right)_{i+1,j}S_{y_{i+1/2,j}} + \left(E_e\right)_{i,j+1}S_{x\,i,j+1/2} + \left(F_e\right)_{i,j+1}S_{y_{i,j+1/2}} + \left(E_e\right)_{i,j}S_{x\,i-1/2,j} + \left(F_e\right)_{i,j}S_{y_{i-1/2,j}}\right]^n;$$

$$Q_{p_{i,j}}^{n+1} = Q_{i,j}^{n} + \Delta Q_{i,j}^{n}; \quad (48)$$

Corrector step:

$$\Delta Q_{ci,j}^{n+1} = -\Delta t_{i,j}/V_{i,j}\left[\left(E_e\right)_{p_{i,j-1}}S_{x\,i,j-1/2} + \left(F_e\right)_{p_{i,j-1}}S_{y_{i,j-1/2}} + \left(E_e\right)_{p_{i,j}}S_{x\,i+1/2,j} + \left(F_e\right)_{p_{i,j}}S_{y_{i+1/2,j}} + \left(E_e\right)_{p_{i,j}}S_{x\,i,j+1/2} + \left(F_e\right)_{p_{i,j}}S_{y_{i,j+1/2}} + \left(E_e\right)_{p_{i-1,j}}S_{x\,i-1/2,j} + \left(F_e\right)_{p_{i-1,j}}S_{y_{i-1/2,j}}\right];$$

$$Q_{i,j}^{n+1} = 0.5\left(Q_{i,j}^{n} + Q_{p_{i,j}}^{n+1} + \Delta Q_{ci,j}^{n+1} - \frac{\Delta t_{i,j}}{V_{i,j}}D\right), \quad (49)$$

where to guarantee numerical stability to the [11] scheme, an artificial dissipation operator, D, is subtracted from the RHS flux terms in the corrector step (see [16]) aiming to eliminate instabilities originated from shock waves. The operator is of $D = d_{i,j}^{(2)} - d_{i,j}^{(4)}$ type, defined in section **3**.

B. MacCormack, 4th Order

[12] extended the standard MacCormack scheme (2nd order accurate in both space and time) to a spatially fourth order accurate scheme. This scheme has a predictor and a corrector stage and the predictor step is described as follows.

Predictor step:

$$(\text{Flux}-2\text{nd})_{i,j}^{n} = \left[\left(E_e\right)_{i,j}S_{x\,i,j-1/2} + \left(F_e\right)_{i,j}S_{y_{i,j-1/2}} + \left(E_e\right)_{i+1,j}S_{x\,i+1/2,j} + \left(F_e\right)_{i+1,j}S_{y_{i+1/2,j}} + \left(E_e\right)_{i,j+1}S_{x\,i,j+1/2} + \left(F_e\right)_{i,j+1}S_{y_{i,j+1/2}} + \left(E_e\right)_{i,j}S_{x\,i-1/2,j} + \left(F_e\right)_{i,j}S_{y_{i-1/2,j}}\right]^n;$$

$$(\text{Flux}-4\text{th})_{i,j}^{n} = \left[\left(E_e\right)_{i,j+1}S_{x\,i,j+1/2} + \left(F_e\right)_{i,j+1}S_{y_{i,j+1/2}} + \left(E_e\right)_{i+2,j}S_{x\,i+3/2,j} + \left(F_e\right)_{i+2,j}S_{y_{i+3/2,j}} + \left(E_e\right)_{i,j+2}S_{x\,i,j+3/2} + \left(F_e\right)_{i,j+2}S_{y_{i,j+3/2}} + \left(E_e\right)_{i+1,j}S_{x\,i+1/2,j} + \left(F_e\right)_{i+1,j}S_{y_{i+1/2,j}}\right]^n;$$

$$Q_{p_{i,j}}^{n+1} = Q_{i,j}^{n} - \frac{\Delta t_{i,j}}{6V_{i,j}}\left[7(\text{Flux}-2\text{nd})_{i,j}^{n} - (\text{Flux}-4\text{th})_{i,j}^{n}\right]; \quad (50)$$

Corrector step:

$$(\text{Flux}-2\text{nd})_{i,j}^{n+1} = \left[\left(E_e\right)_{p_{i,j-1}}S_{x\,i,j-1/2} + \left(F_e\right)_{p_{i,j-1}}S_{y_{i,j-1/2}} + \left(E_e\right)_{p_{i,j}}S_{x\,i+1/2,j} + \left(F_e\right)_{p_{i,j}}S_{y_{i+1/2,j}} + \left(E_e\right)_{p_{i,j}}S_{x\,i,j+1/2} + \left(F_e\right)_{p_{i,j}}S_{y_{i,j+1/2}} + \left(E_e\right)_{p_{i-1,j}}S_{x\,i-1/2,j} + \left(F_e\right)_{p_{i-1,j}}S_{y_{i-1/2,j}}\right];$$

$$(\text{Flux}-4\text{th})_{i,j}^{n+1} = \left[\left(E_e\right)_{p_{i,j-2}}S_{x\,i,j-3/2} + \left(F_e\right)_{p_{i,j-2}}S_{y_{i,j-3/2}} + \left(E_e\right)_{p_{i-1,j}}S_{x\,i-1/2,j} + \left(F_e\right)_{p_{i-1,j}}S_{y_{i-1/2,j}} + \left(E_e\right)_{p_{i,j-1}}S_{x\,i,j-1/2} + \left(F_e\right)_{p_{i,j-1}}S_{y_{i,j-1/2}} + \left(E_e\right)_{p_{i-2,j}}S_{x\,i-3/2,j} + \left(F_e\right)_{p_{i-2,j}}S_{y_{i-3/2,j}}\right];$$

$$Q_{i,j}^{n+1} = 0.5\left\{Q_{i,j}^{n} + Q_{p_{i,j}}^{n+1} - \frac{\Delta t_{i,j}}{6V_{i,j}}\left[7(\text{Flux}-2\text{nd})_{i,j}^{n+1} - (\text{Flux}-4\text{th})_{i,j}^{n+1}\right]\right\} \quad (51)$$

This scheme is second order accurate in time and becomes fourth order accurate in the spatial derivatives when alternated with symmetric variants ([12,19]). Consider L_1 defined as a one dimensional operator with a forward discretization in the predictor and a backward discretization in the corrector. Its symmetric variant L_2 uses a backward discretization in the predictor and a forward discretization in the corrector. Therefore to ensure the fourth order spatial accuracy, the sweeps are arranged in our computations as

$$Q_{i,j}^{n+1} = L_1 Q_{i,j}^{n} \quad (52)$$

$$Q_{i,j}^{n+2} = L_2 Q_{i,j}^{n+1} \quad (53)$$

In the present study, the corrector step is modified to consider the artificial dissipation operator as:

$$Q_{i,j}^{n+1} = 0.5\left\{ Q_{i,j}^{n} + Q_{p_{i,j}}^{n+1} - \frac{\Delta t_{i,j}}{6V_{i,j}}\left[7\left(\text{Flux} - 2\text{nd}\right)_{i,j}^{n+1} - \left(\text{Flux} - 4\text{th}\right)_{i,j}^{n+1} - D_{i,j}^{n+1}\right]\right\} \quad (54)$$

where D is the artificial dissipation operator.

C. Jameson and Mavriplis, 2nd Order

Equation (46) can be rewritten following a structured discretization context ([13,17]) as:

$$d\left(V_{i,j}Q_{i,j}\right)/dt + C(Q_{i,j}) = 0\,, \quad (55)$$

where:

$$\begin{aligned} C(Q_{i,j}) = {} & \left[E_e(Q_{i,j-1/2})S_{x_{i,j-1/2}} + F_e(Q_{i,j-1/2})S_{y_{i,j-1/2}}\right] + \\ & \left[E_e(Q_{i+1/2,j})S_{x_{i+1/2,j}} + F_e(Q_{i+1/2,j})S_{y_{i+1/2,j}}\right] + \\ & \left[E_e(Q_{i,j+1/2})S_{x_{i,j+1/2}} + F_e(Q_{i,j+1/2})S_{y_{i,j+1/2}}\right] + \\ & \left[E_e(Q_{i-1/2,j})S_{x_{i-1/2,j}} + F_e(Q_{i-1/2,j})S_{y_{i-1/2,j}}\right] \end{aligned} \quad (56)$$

is the discrete approximation of the flux integral of Eq. (46). In this work, it was adopted that, for example, the values of primitive variables at the (i,j-1/2) flux interface are obtained from the arithmetical average between the values of the primitive variables in the (i,j) volume and in the (i,j-1) volume.

The spatial discretization proposed by the authors is equivalent to a symmetrical scheme with second order accuracy, on a finite difference context. The introduction of an artificial dissipation operator "D" is necessary to guarantee the numerical stability of the scheme in the presence of, for example, odd-even uncoupled solutions and nonlinear instabilities, like shock waves. So, Equation (55) is rewritten as:

$$d\left(V_{i,j}Q_{i,j}\right)/dt + \left[C(Q_{i,j}) - D(Q_{i,j})\right] = 0\,. \quad (57)$$

The time integration is performed using a hybrid explicit Runge-Kutta method of five stages, with second order accuracy, and can be represented in general form as:

$$\begin{aligned} Q_{i,j}^{(0)} &= Q_{i,j}^{(n)} \\ Q_{i,j}^{(l)} &= Q_{i,j}^{(0)} - \alpha_l \Delta t_{i,j}/V_{i,j}\left[C\left(Q_{i,j}^{(l-1)}\right) - D\left(Q_{i,j}^{(m)}\right)\right], \\ Q_{i,j}^{(n+1)} &= Q_{i,j}^{(l)} \end{aligned} \quad (58)$$

where l = 1,...,5; m = 0 until 1; $\alpha_1 = 1/4$, $\alpha_2 = 1/6$, $\alpha_3 = 3/8$, $\alpha_4 = 1/2$ and $\alpha_5 = 1$. [13] suggests that the artificial dissipation operator should only be evaluated in the first two stages when the Euler equations were solved (m = 0, l = 1 and m = 1, l = 2). This procedure aims CPU time economy and also better smoothing of the numerical instabilities of the discretization based on the hyperbolic characteristics of the Euler equations.

VII. Algorithms in 3D

A. MacCormack, 2nd Order

The explicit time march, using the explicit Euler method applied to Eq. (4), leads to the following expression:

$$Q_{i,j,k}^{n+1} = Q_{i,j,k}^{n} - \Delta t_{i,j,k}/V_{i,j,k}\int_{S_{i,j,k}} (\vec{P}\bullet\vec{n})_{i,j,k}\, dS_{i,j,k}\,. \quad (59)$$

In the discretization of the surface integral, the Eq. (59) can be rewritten as:

$$\begin{aligned} Q_{i,j,k}^{n+1} = Q_{i,j,k}^{n} - {} & \Delta t_{i,j,k}/V_{i,j,k}\left[(\vec{P}\bullet\vec{S})_{i,j-1/2,k} + (\vec{P}\bullet\vec{S})_{i+1/2,j,k} + \right. \\ & (\vec{P}\bullet\vec{S})_{i,j+1/2,k} + (\vec{P}\bullet\vec{S})_{i-1/2,j,k} + \\ & \left. (\vec{P}\bullet\vec{S})_{i,j,k-1/2} + (\vec{P}\bullet\vec{S})_{i,j,k+1/2}\right]^{n}\,. \end{aligned} \quad (60)$$

Discretizing space and time together, following a Lax-Wendroff type method, dividing the resultant algorithm in two integration time steps (one predictor and the other corrector) and adopting a forward spatial discretization to the predictor step and a backward spatial discretization to the corrector step, it is possible to obtain the [11] algorithm, based on a finite volume formulation, as follows bellow:

Predictor step:

$$\begin{aligned} \Delta Q_{i,j,k}^{n} = {} & -\Delta t_{i,j,k}/V_{i,j,k}\left\{\left[(E_e)n_{x_{i,j-1/2,k}} + (F_e)n_{y_{i,j-1/2,k}} + (G_e)n_{z_{i,j-1/2,k}}\right]_{i,j,k} S_{i,j-1/2,k} + \right. \\ & \left[(E_e)n_{x_{i+1/2,j,k}} + (F_e)n_{y_{i+1/2,j,k}} + (G_e)n_{z_{i+1/2,j,k}}\right]_{i+1,j,k} S_{i+1/2,j,k} + \\ & \left[(E_e)n_{x_{i,j+1/2,k}} + (F_e)n_{y_{i,j+1/2,k}} + (G_e)n_{z_{i,j+1/2,k}}\right]_{i,j+1,k} S_{i,j+1/2,k} + \\ & \left[(E_e)n_{x_{i-1/2,j,k}} + (F_e)n_{y_{i-1/2,j,k}} + (G_e)n_{z_{i-1/2,j,k}}\right]_{i,j,k} S_{i-1/2,j,k} + \\ & \left[(E_e)n_{x_{i,j,k-1/2}} + (F_e)n_{y_{i,j,k-1/2}} + (G_e)n_{z_{i,j,k-1/2}}\right]_{i,j,k} S_{i,j,k-1/2} + \\ & \left.\left[(E_e)n_{x_{i,j,k+1/2}} + (F_e)n_{y_{i,j,k+1/2}} + (G_e)n_{z_{i,j,k+1/2}}\right]_{i,j,k+1} S_{i,j,k+1/2}\right\} \end{aligned}$$

$$Q_{p_{i,j,k}}^{n+1} = Q_{i,j,k}^{n} + \Delta Q_{i,j,k}^{n}\,. \quad (61)$$

Corrector step:

$$\Delta Q_{ci,j,k}^{n+1} = -\Delta t_{i,j,k}/V_{i,j,k}\left\{\left[(E_e)n_{x_{i,j-1/2,k}} + (F_e)n_{y_{i,j-1/2,k}} + (G_e)n_{z_{i,j-1/2,k}}\right]^{p}_{i,j-1,k} S_{i,j-1/2,k} + \right.$$
$$\left[(E_e)n_{x_{i+1/2,j,k}} + (F_e)n_{y_{i+1/2,j,k}} + (G_e)n_{z_{i+1/2,j,k}}\right]^{p}_{i,j,k} S_{i+1/2,j,k} +$$
$$\left[(E_e)n_{x_{i,j+1/2,k}} + (F_e)n_{y_{i,j+1/2,k}} + (G_e)n_{z_{i,j+1/2,k}}\right]^{p}_{i,j,k} S_{i,j+1/2,k} +$$
$$\left[(E_e)n_{x_{i-1/2,j,k}} + (F_e)n_{y_{i-1/2,j,k}} + (G_e)n_{z_{i-1/2,j,k}}\right]^{p}_{i-1,j,k} S_{i-1/2,j,k} +$$
$$\left[(E_e)n_{x_{i,j,k-1/2}} + (F_e)n_{y_{i,j,k-1/2}} + (G_e)n_{z_{i,j,k-1/2}}\right]^{p}_{i,j,k-1} S_{i,j,k-1/2} +$$
$$\left.\left[(E_e)n_{x_{i,j,k+1/2}} + (F_e)n_{y_{i,j,k+1/2}} + (G_e)n_{z_{i,j,k+1/2}}\right]^{p}_{i,j,k} S_{i,j,k+1/2}\right\}$$

$$Q_{i,j,k}^{n+1} = 0.5\left(Q_{i,j,k}^{n} + Q_{p_{i,j,k}}^{n+1} + \Delta Q_{c_{i,j,k}}^{n+1} - \frac{\Delta t_{i,j}}{V_{i,j}} D \right). \quad (62)$$

An artificial dissipation operator of second and fourth differences (see [16]) is subtracted from the RHS flux terms in the corrector step aiming to provide numerical stability in the proximities of shock waves and uncoupled solutions.

B. Jameson and Mavriplis, 2nd Order

The Equation (4) can be rewritten as follows:

$$d(Q_{i,j,k})/dt + 1/V_{i,j,k}\left[(\vec{P}\bullet\vec{S})_{i,j-1/2,k} + (\vec{P}\bullet\vec{S})_{i+1/2,j,k} + (\vec{P}\bullet\vec{S})_{i,j+1/2,k} + (\vec{P}\bullet\vec{S})_{i-1/2,j,k} + (\vec{P}\bullet\vec{S})_{i,j,k-1/2} + (\vec{P}\bullet\vec{S})_{i,j,k+1/2}\right]^{n} = 0. \quad (63)$$

The inviscid flux vectors in each flux interface are implemented considering the arithmetical average of the primitive variables in each face; in other words, to the flux face (i,j-1/2,k) is possible to determine the primitive variables at interface using arithmetical average between values of the primitive variable of the volumes (i,j-1,k) and (i,j,k):

$$\rho_{i,j-1/2,k} = 0.5(\rho_{i,j-1,k} + \rho_{i,j,k});$$
$$u_{i,j-1/2,k} = 0.5(u_{i,j-1,k} + u_{i,j,k});$$
$$v_{i,j-1/2,k} = 0.5(v_{i,j-1,k} + v_{i,j,k});$$
$$w_{i,j-1/2,k} = 0.5(w_{i,j-1,k} + w_{i,j,k});$$
$$e_{i,j-1/2,k} = 0.5(e_{i,j-1,k} + e_{i,j,k}). \quad (64)$$

The spatial discretization proposed by the authors is symmetrical on the context of a finite difference technique. With the purpose of avoiding uncoupled solutions, nonlinear instabilities (shock waves), etc., it is explicitly introduced an artificial dissipation operator "D" to provide scheme numerical stability. So, Equation (63) can be rewritten as:

$$d(Q_{i,j,k})/dt + 1/V_{i,j,k}\left[C(Q_{i,j,k}) - D(Q_{i,j,k})\right] = 0, \quad (65)$$

where:

$$C(Q_{i,j,k}) = \left[(P\cdot S)_{i,j-1/2,k} + (P\cdot S)_{i+1/2,j,k} + (P\cdot S)_{i,j+1/2,k} + (P\cdot S)_{i-1/2,j,k} + (P\cdot S)_{i,j,k-1/2} + (P\cdot S)_{i,j,k+1/2}\right]^{n} \quad (66)$$

is the flux integral to the cell (i,j,k).

The time integration is performed using a hybrid explicit Runge-Kutta method with first or second order of accuracy. The more general form of this method is presented below, where the values of the α coefficients are chosen to provide first or second order of time accuracy, as well as to invest certain properties to the scheme which benefit the use of the "multigrid" convergence acceleration technique.

$$Q_{i,j,k}^{(0)} = Q_{i,j,k}^{n}$$
$$Q_{i,j,k}^{(l)} = Q_{i,j,k}^{(0)} - \alpha_l \Delta t_{i,j,k}/V_{i,j,k}\left[C(Q_{i,j,k}^{(l-1)}) - D(Q_{i,j,k}^{(m)})\right], \quad (67)$$
$$Q_{i,j,k}^{n+1} = Q_{i,j,k}^{(l)}$$

where "l" varies from 1 to 5; "m" varies according to the type of the studied flow (inviscid or viscous). As reported in section **6.3**, [13] suggests that the artificial dissipation should be evaluated in the first two stages when the Euler equations were solved (m = 1 and 2, in the five stage case). This procedure aims to allow a CPU time economy and also better smooth of the numerical instabilities of the discretization based on the hyperbolic characteristics of the Euler equations. The α numbers assume the following values: $\alpha_1 = 1/4$, $\alpha_2 = 1/6$, $\alpha_3 = 3/8$, $\alpha_4 = 1/2$, $\alpha_5 = 1.0$.

VIII. SPATIALLY VARIABLE TIME STEP

The idea of a spatially variable time step consists in keeping constant a CFL number in the calculation domain and to guarantee time steps appropriated to each mesh region during the convergence process. The spatially variable time step can be defined in 3D by:

$$\Delta t_{i,j,k} = \frac{CFL(\Delta s)_{i,j,k}}{(|q| + a)_{i,j,k}}, \quad (68)$$

where CFL is the Courant number to method stability; $(\Delta s)_{i,j,k}$ is a characteristic length of information transport; and $(|q| + a)_{i,j,k}$ is the maximum characteristic velocity of information transport, where "a" is the speed of sound. The characteristic length of information transport, $(\Delta s)_{i,j,k}$, can be determined by:

$$(\Delta s)_{i,j,k} = \left[MIN(l_{MIN}, C_{MIN})\right]_{i,j,k}, \quad (69)$$

where lMIN is the minimum side length which forms a computational cell and CMIN is the minimum distance of baricenters between the computational cell and its neighbours, in three dimensions, or the minimum distance of centroids beteween the computational cell and its neighbours, in two-dimensions. The maximum characteristic speed of information transport is defined by $\left(|q| + a\right)_{i,j,k}$, with $q = \sqrt{u^2 + v^2 + w^2}$, in three-dimensions, or $q = \sqrt{u^2 + v^2}$, in two-dimensions.

IX. Initial and Boundary Conditions

A. Initial Condition

To the physical problems studied in this work, freestream flow values are adopted for all properties as initial condition, in the whole calculation domain ([13,18]). Therefore, the vector of conserved variables for two-dimensions is defined as:

$$Q_{i,j} = \left\{1 \quad M_\infty \cos\alpha \quad M_\infty \sin\alpha \quad \frac{1}{\gamma(\gamma-1)} + 0.5M_\infty^2\right\}^T, \quad (70)$$

being M∞ the freestream flow Mach number and α the flow attack angle.

B. Boundary Conditions

The boundary conditions are basically of four types: solid wall, entrance, exit and lateral planes. These conditions are implemented in special cells named ghost cells.

Wall condition: This condition imposes the flow tangency at the solid wall. This condition is satisfied considering the wall tangent velocity component of the ghost volume as equals to the respective velocity component of its real neighbour cell. At the same way, the wall normal velocity component of the ghost cell is equaled in value, but with opposite signal, to the respective velocity component of the real neighbour cell.

The pressure gradient normal to the wall is assumed be equal to zero, following an inviscid formulation. The same hypothesis is applied to the temperature gradient normal to the wall, considering adiabatic wall. The ghost volume density and pressure are extrapolated from the respective values of the real neighbour volume (zero order extrapolation), with these two conditions. The total energy is obtained by the state equation of a perfect gas.

Entrance condition:
(1) Subsonic flow: Three properties are specified and one is extrapolated, based on analysis of information propagation along characteristic directions in the calculation domain ([18]). In other words, three characteristic directions of information propagation point inward the computational domain and should be specified. Only the characteristic direction associated to the "(qn-a)" velocity cannot be specified and should be determined by interior information of the calculation domain. The pressure was the extrapolated variable from the real neighbour volume, to the studied problems. Density and velocity components had their values determined by the freestream flow properties. The total energy per unity fluid volume is determined by the state equation of a perfect gas. For three-dimensions, four properties are specified and one is extrapolated. The pressure is the extrapolated variable, whereas the density and velocity components are fixed.
(2) Supersonic flow: All variables are fixed with their freestream flow values.

Exit condition:
(1) Subsonic flow: Three characteristic directions of information propagation point outward the computational domain and should be extrapolated from interior information ([18]). The characteristic direction associated to the "(qn-a)" velocity should be specified because it penetrates the calculation domain. In this case, the ghost volume's pressure is specified by its freestream value. Density and velocity components are extrapolated and the total energy is obtained by the state equation of a perfect gas. For three-dimensions, four properties are extrapolated, density and velocity components, and the pressure is fixed.
(2) Supersonic flow: All variables are extrapolated from the interior domain due to the fact that all four, or five, characteristic directions of information propagation of the Euler equations point outward the calculation domain and, with it, nothing can be fixed.

Lateral Planes: The lateral boundaries in three-dimensions consider flow tangency condition at these frontiers. Pressure and density are extrapolated from the internal flow. Energy is obtained from the perfect gas equation.

X. Results

A. Geometry and Meshes

Figure 1 exhibits the compression corner configuration employed in this work. This physical problem presents a convex corner which generates an oblique shock wave extending from the corner. Figure 2 shows the two-dimensional mesh, whereas Fig. 3 shows the three-dimensional mesh. The former is constituted of 70x50 points, which is equivalent of being composed of 3,381 rectangular cells and 3,500 nodes, equally spaced. On the other hand, the latter is constituted of 70x50x10 points, which is equivalent of being composed of 30,429 hexahedron cells and 35,000 nodes, equally spaced.

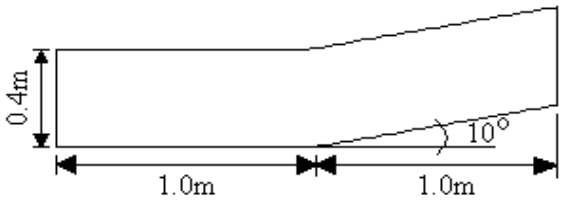

Figure 1. Corner configuration (2D and 3D).

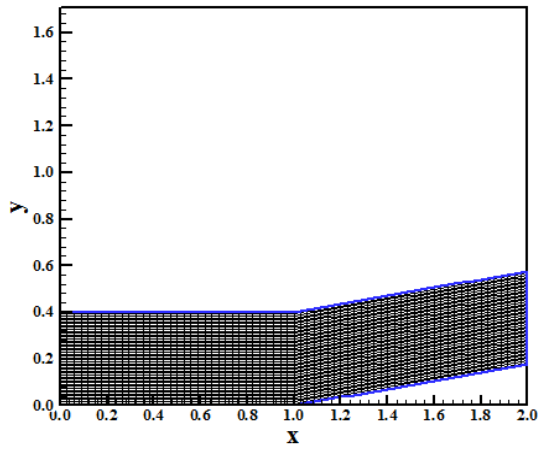

Figure 2. Two-dimensional corner mesh.

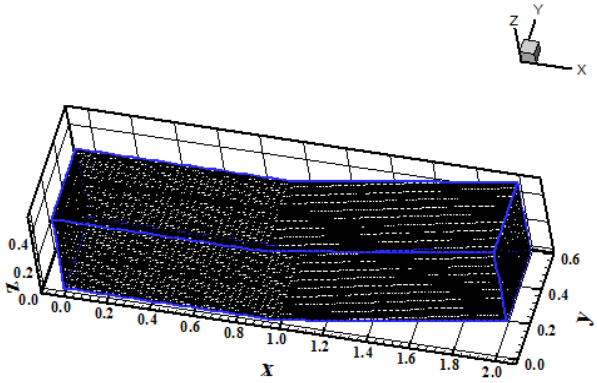

Figure 3. Three-dimensional corner mesh.

B. *Two-Dimensional Results*

Figures 4 to 6 shows the pressure contours obtained by the [11], [12] and [13] numerical schemes, respectively, as using the [8] artificial dissipation model. As can be observed, the [12] solution presents some pressure oscillations close to the corner. However, the minimum shock wave thickness is captured by the [12] scheme. The most severe pressure field is obtained by the [13] scheme.

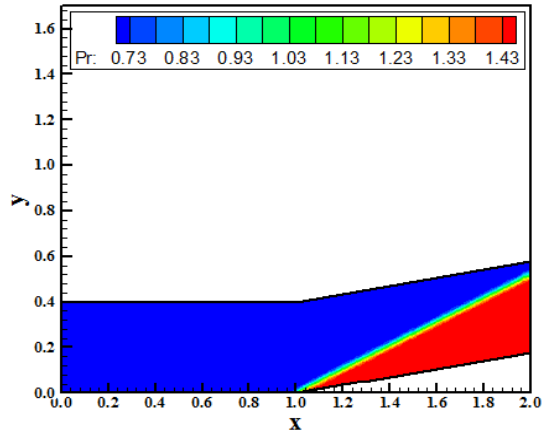

Figure 4. Pressure contours ([11]-[8]).

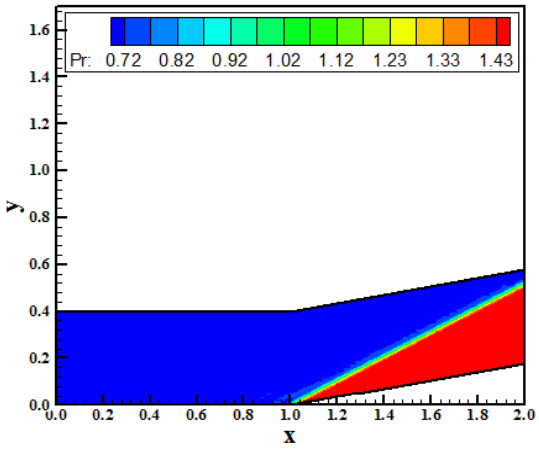

Figure 5. Pressure contours ([12]-[8]).

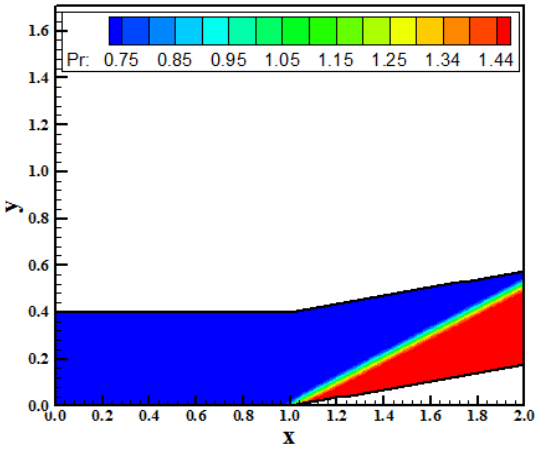

Figure 6. Pressure contours ([13]-[8]).

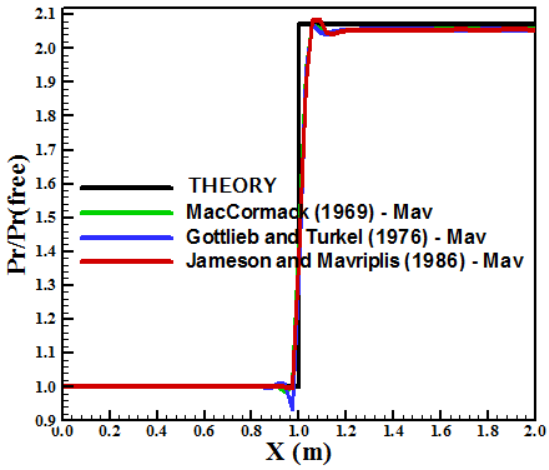

Figure 7. Pressure distributions at wall (Mav).

Figure 7 presents the pressure distributions at the wall obtained by the [11-13] numerical schemes as using the [8] dissipation operator. The best pressure distribution is that obtained by the [13] algorithm, in spite of the oscillation at the corner.

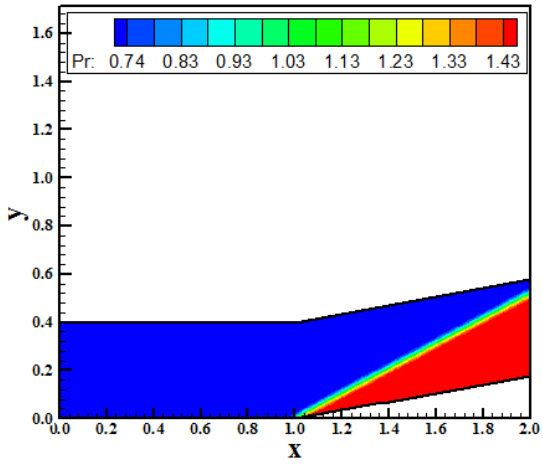

Figure 8. Pressure contours ([11]-[9]).

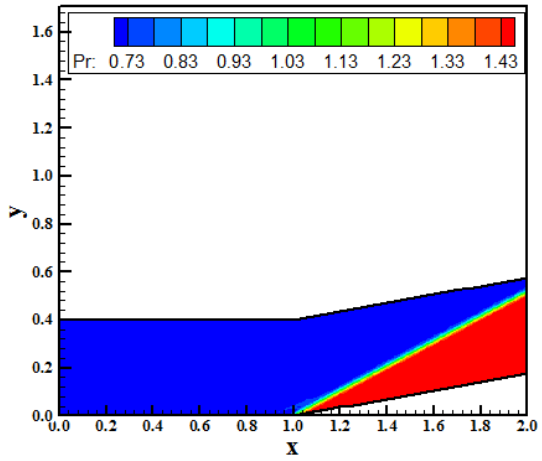

Figure 9. Pressure contours ([12]-[9]).

Figures 8 to 10 exhibit the pressure contours obtained by the [11], [12] and [13] numerical schemes. The most severe pressure field is obtained by the [13] scheme. Again, the minimum shock wave thickness is obtained by the [12] scheme, which presents small pressure oscillations close to the corner.

Figure 11 shows the wall pressure distributions of the three schemes as using the [9] artificial dissipation model. Again, the [13] algorithm predicts the best pressure distribution at the wall. The [12] scheme predicts this distribution with an oscillation at the corner.

Figures 12 to 14 present the pressure contours resulting from the [11], [12] and [13] schemes, respectively, as using the [10] dissipation model. The [12] solution presents pressure oscillations ahead of the corner, whereas the [13] solution presents problems at the corner top. The minimum shock wave thickness is captured by all three schemes. The most severe pressure field is obtained by the [12] algorithm.

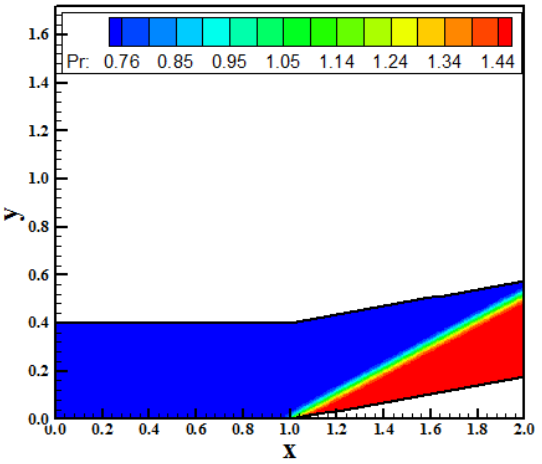

Figure 10. Pressure contours ([13]-[9]).

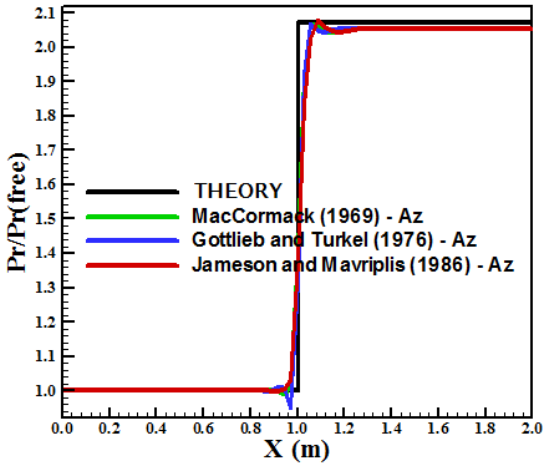

Figure 11. Pressure distributions at wall (Az).

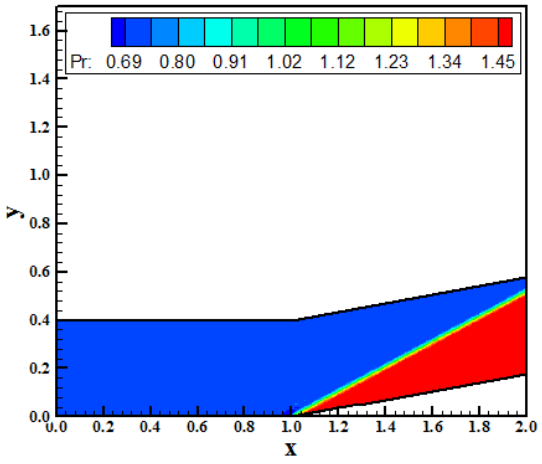

Figure 12. Pressure contours ([11]-[10]).

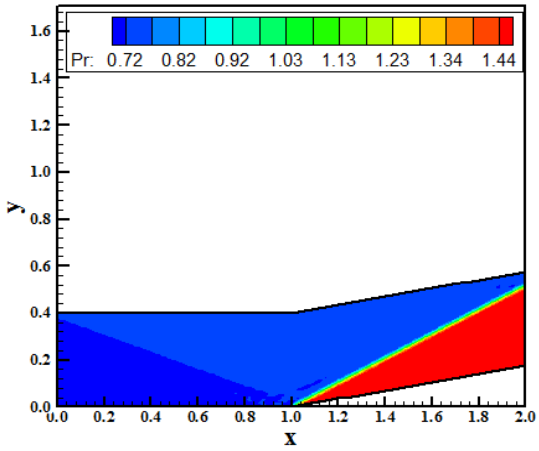

Figure 13. Pressure contours ([12]-[10]).

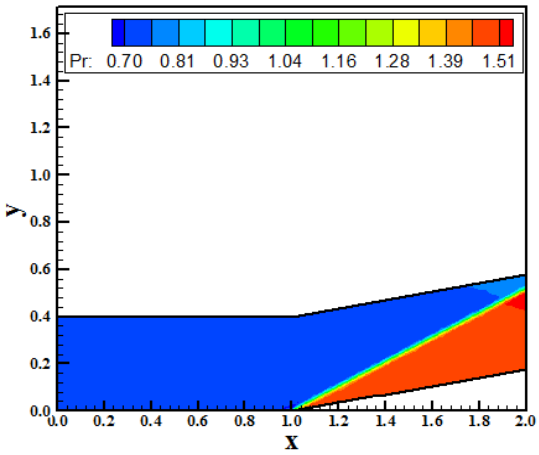

Figure 14. Pressure contours ([13]-[10]).

Figure 15 shows the wall pressure distribution generated along the compression corner by the [11], [12] and [13] schemes, respectively, as using the [10] dissipation model. The best pressure distribution, close to the pressure profile, is due to [12] scheme.

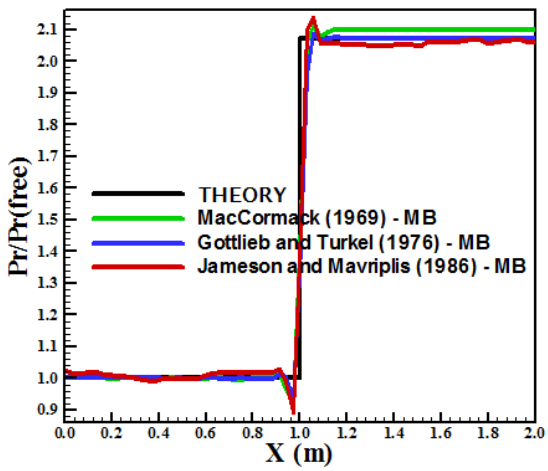

Figure 15. Pressure distributions at wall (MB).

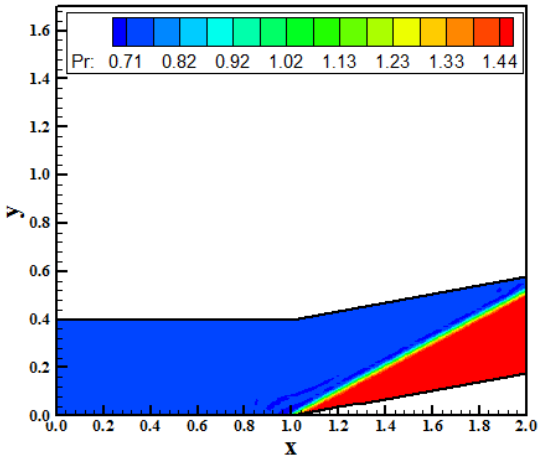

Figure 16. Pressure contours ([11]-[3]-S).

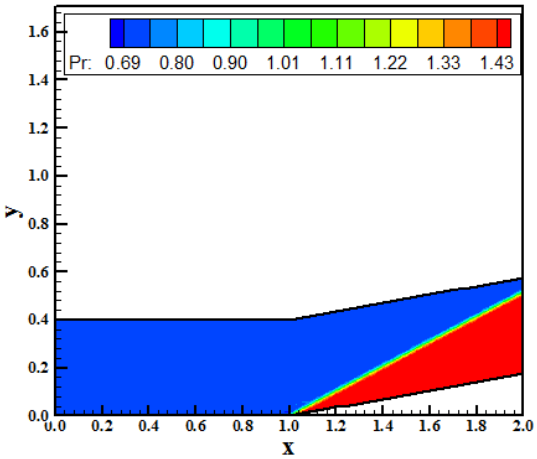

Figure 17. Pressure contours ([12]-[3]-S).

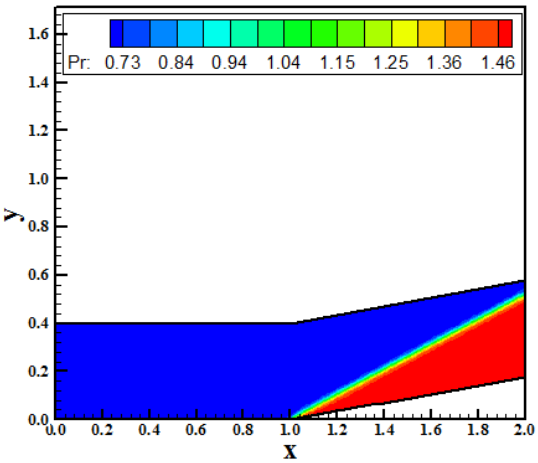

Figure 18. Pressure contours ([13]-[3]-S).

Figures 16 to 18 exhibit the pressure contours generated at the compression corner obtained by the [11-13] schemes, respectively. The lowest shock wave thickness is obtained by the [12] scheme. It seems that the fourth order accuracy of this

scheme really provides good solution characteristics in qualitative terms, capturing the best shock wave thickness. It is also obvious that the dissipation model has a great influence in this solution. It is clear that the anisotropic properties of this dissipation model is the great responsible to so good behavior of the [12] scheme. The [11] scheme presents oscillations close to the corner and the [13] scheme presents thicker shock wave thickness, using this same dissipation model.

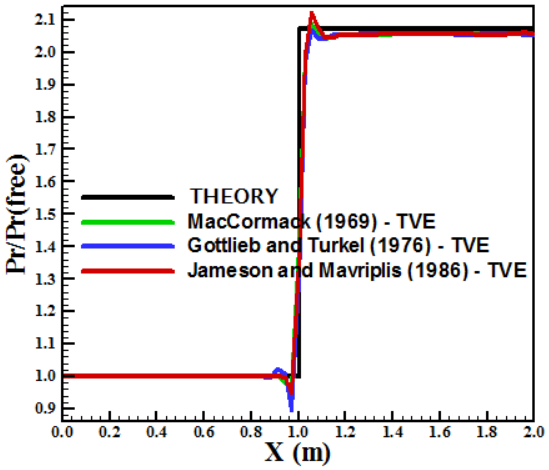

Figure 19. Pressure distributions at wall (TVE).

Therefore, the [12] scheme has its merits to capture appropriately the shock wave. Figure 19 exhibits the wall pressure distributions of the three schemes along the compression corner. The best behavior is due to the [11] scheme as using the [3] scalar dissipation model. Some overshoots and undershoots are presented in the solutions and the best behavior is observed with the [11] algorithm.

Figures 20 to 22 present the pressure contours obtained by the [11-13] algorithms as using the [3] matrix model. The best prediction of the shock wave thickness is again observed with the [12] algorithm. In all solutions oscillations are present.

All schemes present the minimum shock wave thickness in relation to the other models. The matrix model is the best in this prediction.

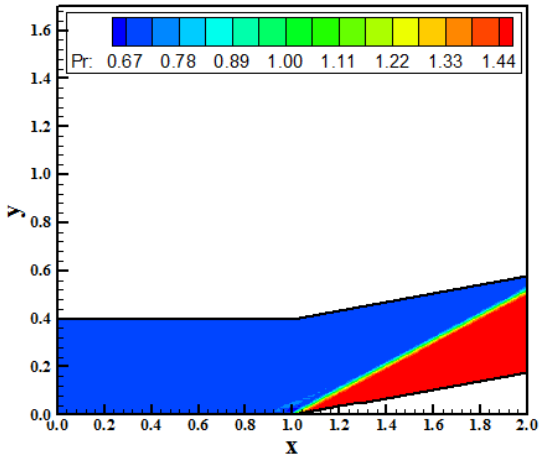

Figure 20. Pressure contours ([11]-[3]-M).

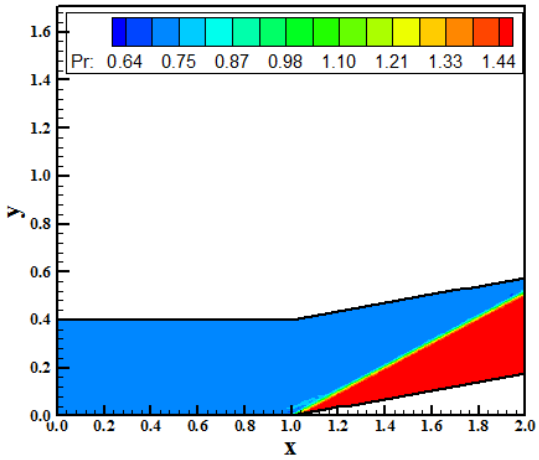

Figure 21. Pressure contours ([12]-[3]-M).

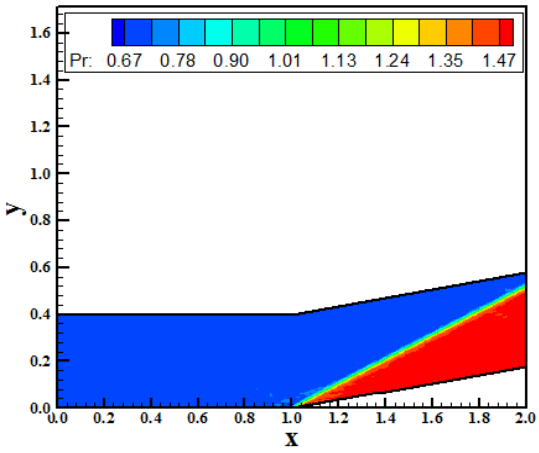

Figure 22. Pressure contours ([13]-[3]-M).

Figure 23 shows the pressure distributions at the wall generated by the [11], [12] and [13] schemes, respectively, as using the [3] matrix model. The best pressure distribution is due to the [11] scheme. All schemes present overshoots and undershoots.

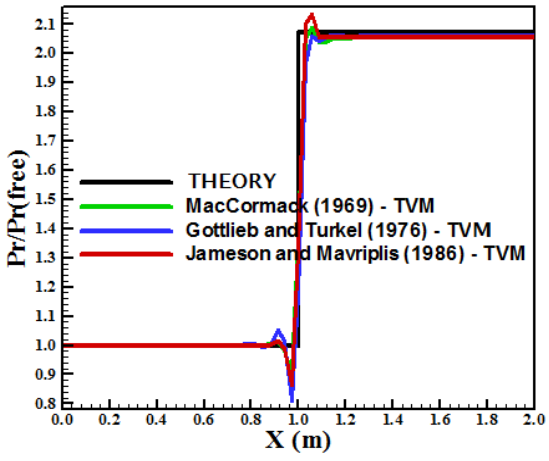

Figure 23. Pressure distributions at wall (TVM).

As conclusion in qualitative terms, considering two-dimensional simulations, the [12] scheme was the best in the prediction of shock wave thickness. Moreover, the matrix model is the best in the prediction of the shock wave thickness. The best wall pressure distribution was due to [11].

C. *Three-Dimensional Results*

Figures 24 and 25 exhibit the pressure contours obtained by the [11,13] algorithms, respectively. Both solutions are clear. Only small oscillations are perceptible close to the corner. Both solutions present the same shock wave thickness.

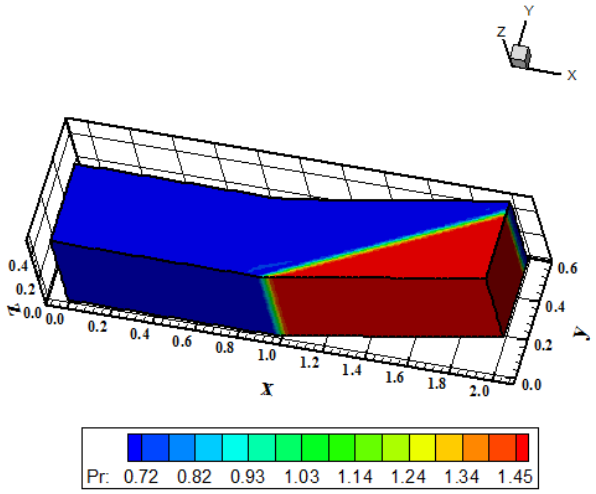

Figure 24. Pressure contours ([11]-[8]).

The most severe pressure field is due to [13] scheme. Figure 26 exhibits the wall pressure distributions obtained by the [11] and [13] schemes. Both solutions are very close, but the [11] scheme is better than the [13] scheme, presenting minimum undershoots and overshoots.

Figures 27 and 28 shows the pressure contours obtained by the [11,13] schemes, respectively, as using the [9] dissipation model. Both solutions present the same shock wave thickness. The most severe pressure field is due to [13] scheme.

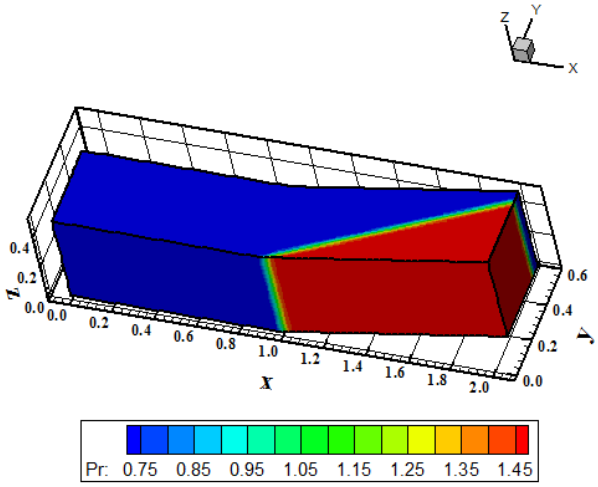

Figure 25. Pressure contours ([13]-[8]).

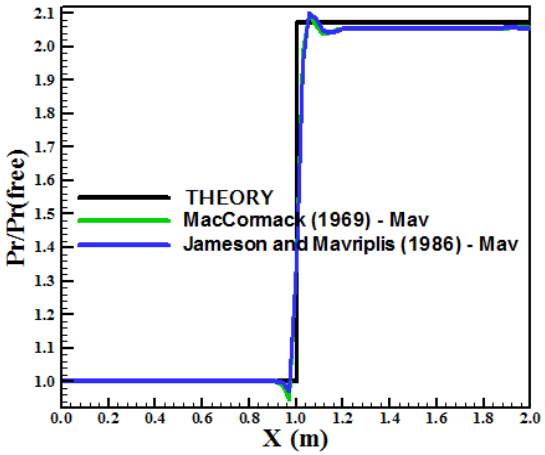

Figure 26. Pressure distributions at wall (Mav).

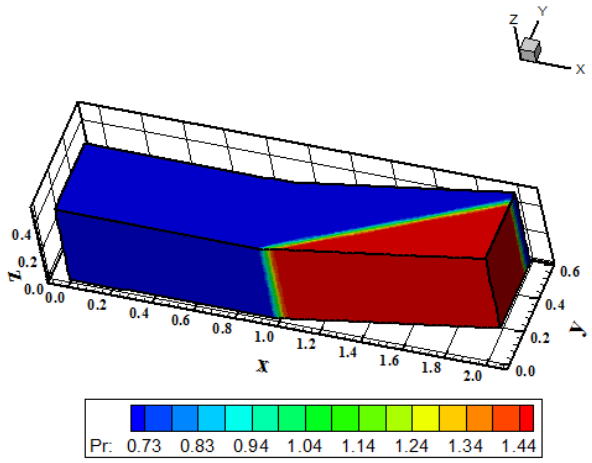

Figure 27. Pressure contours ([11]-[9]).

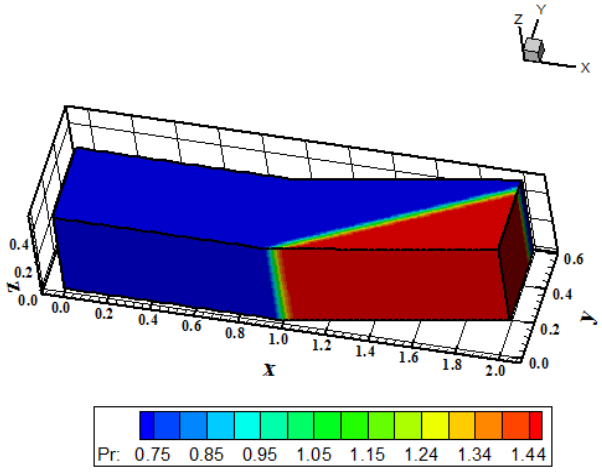

Figure 28. Pressure contours ([13]-[9]).

Figure 29 presents the wall pressure distributions along the compression corner obtained by the [11] and [13] algorithms as using the [9] dissipation model. The best pressure profile is due to [13] algorithm.

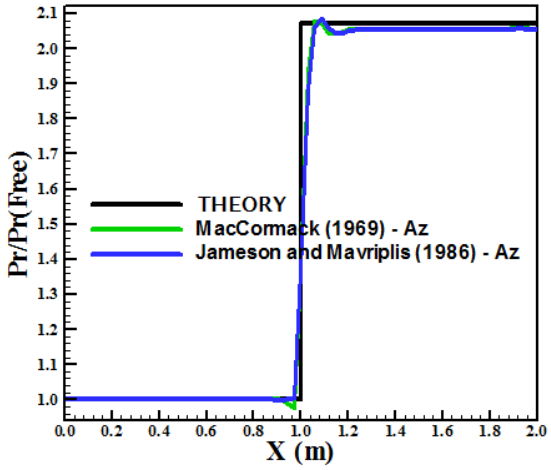

Figure 29. Pressure distributions at wall (Az).

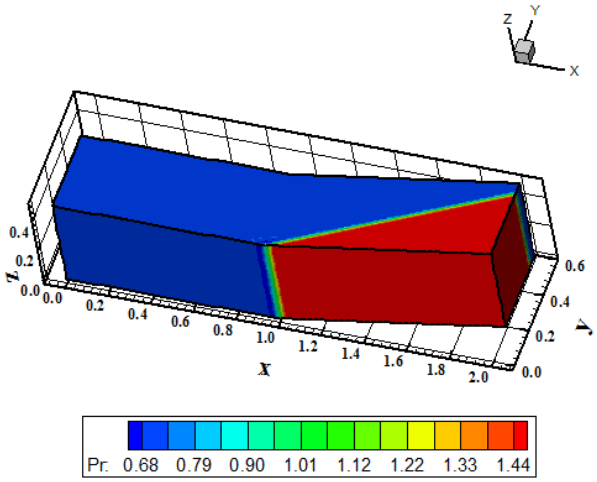

Figure 30. Pressure contours ([11]-[10]).

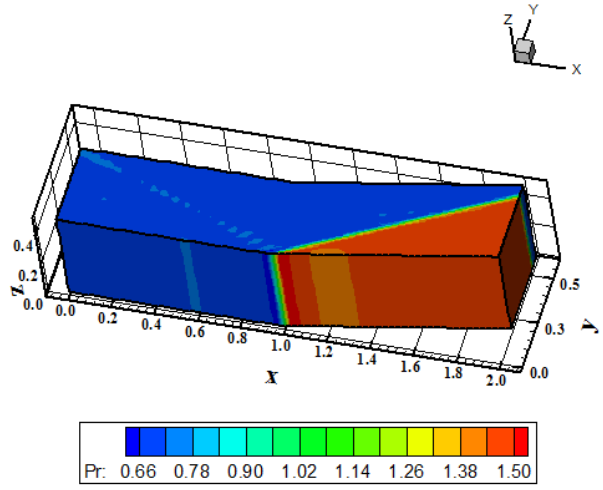

Figure 31. Pressure contours ([13]-[10]).

Figures 30 and 31 exhibit the pressure contours obtained by the [11] and [13] schemes, respectively, as using the [10] dissipation model. Here is a new paradigm. The [10] dissipation model provides better shock wave thickness than the other models tested herein. Both solutions present this aspect, although the [13] solution presents pressure oscillations at the field. The most severe pressure field is due to [11] scheme.

Figure 32 shows the wall pressure distributions along the compression corner generated by the [11,13] schemes. The better prediction is due to the [11] algorithm using this dissipation model.

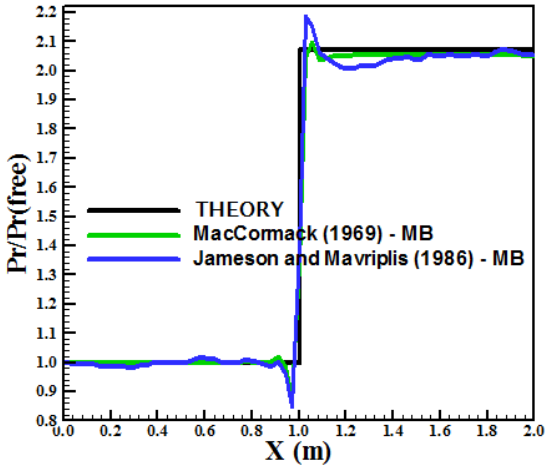

Figure 32. Pressure distributions at wall (MB).

Figures 33 and 34 exhibit the pressure contours generated by the [11,13] schemes, respectively, as using the [3] scalar dissipation model. Only the [11] solution presents homogeneity properties in the shock wave region. On the other hand, the [13] solution spread out the post-shock properties in the field. The shock wave thicknesses of the [10] model are better than the present ones. The most severe pressure field is due to the [13] algorithm.

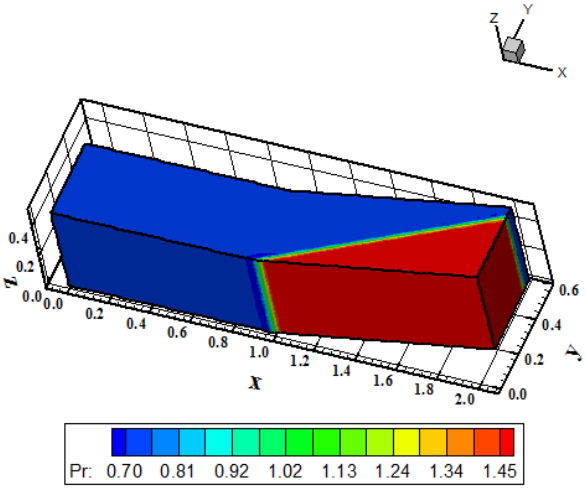

Figure 33. Pressure contours ([11]-[3]-S).

Figure 35 shows the wall pressure distributions obtained by the [11] and [13] algorithms. Both solutions present under- and overshoots, but the best behavior is observed with the [11] scheme (minor oscillation sizes).

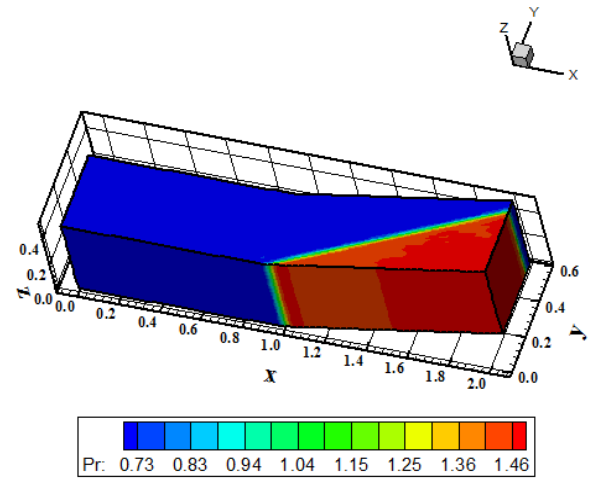

Figure 34. Pressure contours ([13]-[3]-S).

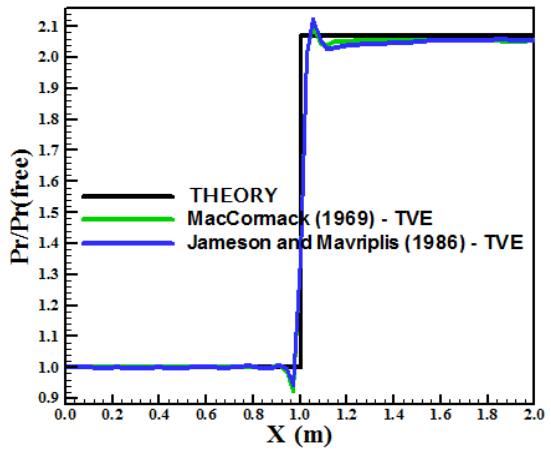

Figure 35. Pressure distributions at wall (TVE).

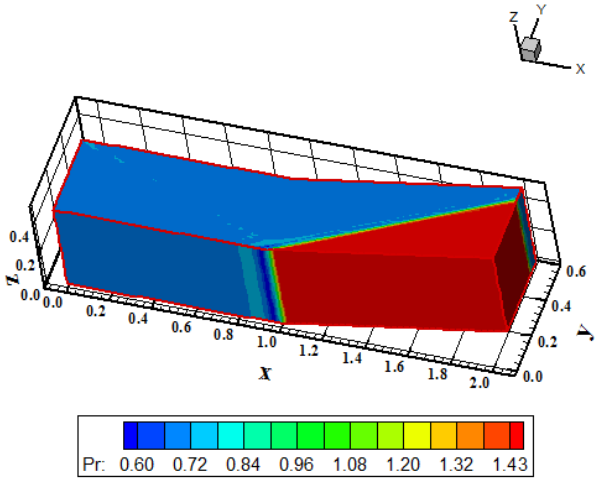

Figure 36. Pressure contours ([11]-[3]-M).

Figures 36 and 37 present the pressure contours generated by the [11] and by the [13] algorithms, respectively, as using the [3] matrix model. The shock wave thickness is minimum in both solutions, minimum than the other models, highlighting this artificial dissipation model as the best of the studied herein. Some pressure oscillations are present in both solutions, but the homogeneity property is better observed in the [11] solution. Figure 38 exhibit the wall pressure distributions along the compression corner obtained by [11,13] schemes. The better prediction is due to the [11] model.

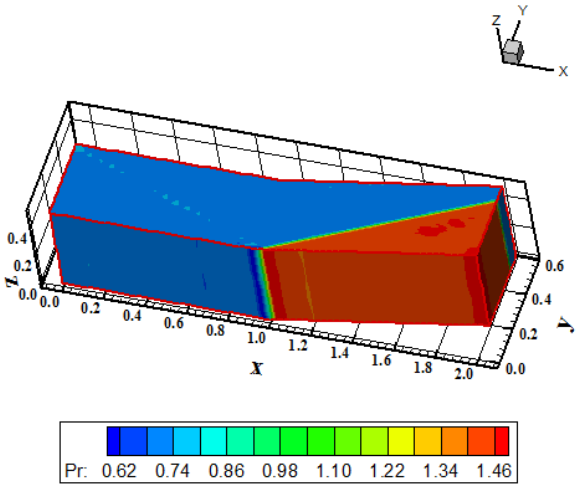

Figure 37. Pressure contours ([13]-[3]-M).

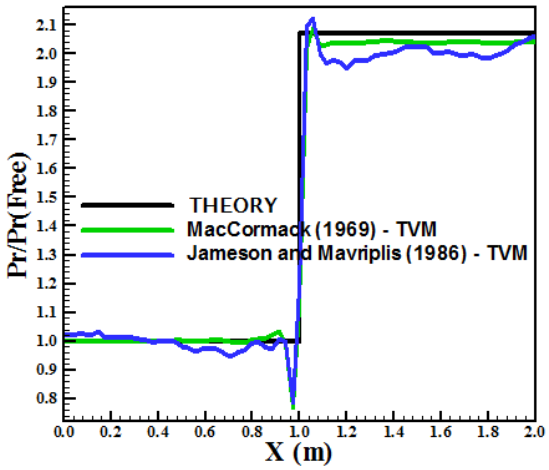

Figure 38. Pressure distributions at wall (TVM).

As conclusion of the three-dimensional study, the best dissipation model to predict the minimum shock wave thickness was due to [3] matrix model. The best pressure profile was obtained in all cases by the [11] scheme.

D. Quantitative Results

One way to quantitatively verify if the solutions generated by each scheme are satisfactory consists in determining the shock angle of the oblique shock wave, β, measured in relation to the initial direction of the flow field. [20] (pages 352 and 353) presents a diagram with values of the shock angle, β, to oblique shock waves. The value of this angle is determined as function of the freestream Mach number and of the deflection angle of the flow after the shock wave, ϕ. To ϕ = 10º (corner inclination angle) and to a freestream Mach number equals to 3.0, it is possible to obtain from this diagram a value to β equals to 27.5º.

Table 1. Shock angle and percentage errors.

Case	Scheme	Model	β (°)	Error %
2D	[11]	[8]	27.8	1.09
2D	[12]	[8]	27.9	1.45
2D	[13]	[8]	27.7	0.73
2D	[11]	[9]	27.5	0.00
2D	[12]	[9]	27.6	0.36
2D	[13]	[9]	27.4	0.36
2D	[11]	[10]	27.5	0.00
2D	[12]	[10]	27.6	0.36
2D	[13]	[10]	27.4	0.36
2D	[11]	[3]-S	28.0	1.82
2D	[12]	[3]-S	27.5	0.00
2D	[13]	[3]-S	27.8	1.09
2D	[11]	[3]-M	27.5	0.00
2D	[12]	[3]-M	27.5	0.00
2D	[13]	[3]-M	27.9	1.45
3D	[11]	[8]	27.5	0.00
3D	[13]	[8]	27.5	0.00
3D	[11]	[9]	27.5	0.00
3D	[13]	[9]	28.0	1.82
3D	[11]	[10]	27.3	0.73
3D	[13]	[10]	27.5	0.00
3D	[11]	[3]-S	27.5	0.00
3D	[13]	[3]-S	27.6	0.36
3D	[11]	[3]-M	26.9	2.18
3D	[13]	[3]-M	26.9	2.18

Using a transfer in the pressure contours, it is possible to obtain the values of β to each scheme, as well the respective errors, shown in Tab. 1. For the three-dimensional case, the pressure contours were studied at the xy plane.

The best result for the two-dimensional case, considering each dissipation model, was due to the [3] matrix model because it reproduces the exact value of the shock angle in two solutions, [11] and [12] schemes, and presents a small error with the [13] scheme (< 1.50%). For the three-dimensional case, the best dissipation model was the [8] dissipation model because it reproduces the exact value in two solutions, [11] and [13] algorithms. The Turkel and Vatsa's matrix model was the best in the two-dimensional case, whereas the Mavriplis' model was the best in the three-dimensional case. The best scheme was the [12] algorithm in the two-dimensional case, whereas is the [11] algorithm in the three-dimensional case. In general, the errors obtained with the results were inferior to 2.50%, which is an excellent result considering that the schemes are not of high resolution.

XI. Conclusions

In this paper, the Euler equations in conservative and integral forms are applied to the solution of the supersonic flow along a compression corner. Five artificial dissipation models are tested, aiming to identify the main vantages and disadvantages of each one. Three isotropic models based on the works of [8], [9], and [10] are implemented. On the other hand, two anisotropic models based on the work of [3] are studied. The isotropic models are scalar ones, whereas the anisotropic models are scalar and matrix ones. Such studies are performed on a finite volume and structured contexts, in two- and three-dimensional spaces. The algorithms to perform the numerical experiments are the [11], second order, the [12], fourth order, and the [13], second order, in two-dimensions. In three-dimensions, one studies the [11], second order, and the [13], second order. All schemes are predictor-corrector or symmetrical ones. Convergence is accelerated to steady state by a spatially variable time step procedure, which has proved excellent results as reported by [14-15]. Good results are obtained by all models, especially for the matrix model, and are reported in this paper.

The best result for the two-dimensional case, considering each dissipation model, was due to the [3] matrix model because it reproduces the exact value of the shock angle in two solutions, [11] and [12] schemes, and presents a small error with the [13] scheme (< 1.50%). For the three-dimensional case, the best dissipation model was the [8] dissipation model because it reproduces the exact value in two solutions, [11] and [13] algorithms. The Turkel and Vatsa's matrix model was the best in the two-dimensional case, whereas the Mavriplis' model was the best in the three-dimensional case.

The best scheme was the [12] algorithm in the two-dimensional case, whereas is the [11] algorithm in the three-dimensional case. In general, the errors obtained with the results were inferior to 2.50%, which is an excellent result considering that the schemes are not of high resolution.

References

[1] D. W. Zingg, "Grid Studies for Thin-Layer Navier-Stokes Computations of Airfoil Flowfields", *AIAA Journal*, Vol. 30, No. 10, pp. 2561-2564, 1992.

[2] C. McNeil, "The Effect of Numerical Dissipation on High Reynolds Number Turbulent Flow Solutions", *AIAA Paper 96-0891*, 1996.

[3] E. Turkel, and V. N. Vatsa, "Effect of Artificial Viscosity on Three-Dimensional Flow Solutions", *AIAA Journal*, Vol. 32, No. 1, pp. 39-45, 1994.

[4] S. R. Allmaras, "Contamination of Laminar Boundary Layers by Artificial Dissipation in Navier-Stokes Solutions", *Numerical Methods for Fluid Dynamics*, M. J. Baines and K. W. Morton, eds., Clarendon Press, Oxford, 1993.

[5] S. Reddy, and M. Papadakis, "Artificial Viscosity Models for the Navier-Stokes Equations and Their Effect in Drag Prediction", *AIAA Paper 93-0193*, 1993.

[6] J. Wen-Huei, L. B. Wigton, S. R. Allmaras, P. R. Spalart, and N. J. Yu, "Towards Industrial-Strength Navier-Stokes Codes", *Numerical and Physical Aspects of Aerodynamic Flows V*, T. Cebeci, ed., Springer Verlag, 1992.

[7] R. P. Varma, and D. A. Caughey, "Estimation of the Integrated Effect of Numerical Dissipation on Navier-Stokes Solutions", *Fourth International Symposium on Computational Fluid Dynamics*, Davis, Sept. 1991.

[8] D. J. Mavriplis, "Accurate Multigrid Solution of the Euler Equations on Unstructured and Adaptive Meshes", *AIAA Journal*, Vol. 28, No. 2, pp. 213-221, 1990.

[9] J. L. F. Azevedo, "On the Development of Unstructured Grid Finite Volume Solvers for High Speed Flows", *NT-075-ASE-N*, IAE, CTA, São José dos Campos, SP, Brasil, 1992.

[10] R. W. MacCormack, and B. S. Baldwin, "A Numerical Method for Solving the Navier-Stokes Equations with Application to Shock Boundary layer Interactions", *AIAA Paper 75-1*, 1975.
[11] R. W. MacCormack, R. W., "The Effect of Viscosity in Hypervelocity Impact Cratering", *AIAA Paper 69-354*, 1969.
[12] D. Gottlieb, and E. Turkel, "Dissipative Two-Four Methods for Time Dependent Problems", *Math. Comp.*, Vol. 30, pp 703-723, 1976.
[13] A. Jameson, and D. J. Mavriplis, "Finite Volume Solution of the Two-Dimensional Euler Equations on a Regular Triangular Mesh", *AIAA Journal*, Vol. 24, No. 4, pp. 611-618, 1986.
[14] E. S. G. Maciel, "Analysis of Convergence Acceleration Techniques Used in Unstructured Algorithms in the Solution of Aeronautical Problems – Part I", *Proceedings of the XVIII International Congress of Mechanical Engineering (XVIII COBEM)*, Ouro Preto, MG, Brazil, 2005.
[15] E. S. G. Maciel, "Analysis of Convergence Acceleration Techniques Used in Unstructured Algorithms in the Solution of Aerospace Problems – Part II", *Proceedings of the XII Brazilian Congress of Engineering and Thermal Sciences (XII ENCIT)*, Belo Horizonte, MG, Brasil, 2008.
[16] E. S. G., Maciel, "Comparação entre Diferentes Modelos de Dissipação Artificial Aplicados a um Sistema de Coordenadas Generalizadas – Parte I", *Proceedings of the 7th Symposium of Computational Mechanics (VII SIMMEC)*, Araxá, MG, Brazil, 2006.
[17] A. Jameson, W. Schmidt, and E. Turkel, 1981, "Numerical Solution for the Euler Equations by Finite Volume Methods Using Runge-Kutta Time Stepping Schemes", *AIAA Paper 81-1259*, 1981.
[18] E. S. G. Maciel, "Simulação Numérica de Escoamentos Supersônicos e Hipersônicos Utilizando Técnicas de Dinâmica dos Fluidos Computacional", Ph.D. dissertation, ITA, CTA, São José dos Campos, SP, Brazil, 258p, 2002.
[19] M. E. Hyder, and E. Turkel, "High Order Accurate Solutions of Viscous Problems", *AIAA Paper 93-3074*, *NASA TM 106267*, 1993.
[20] J. D. Anderson Jr., *Fundamentals of Aerodynamics*, McGraw-Hill, Inc., EUA, 563p., 1984.

Edisson S. G. Maciel (F'14), born in 1969, february, 25, in Recife, Pernambuco. He is a Mechanical Engineering undergraduated by UFPE in 1992, in Recife, PE, Brazil; Mester degree in Thermal Engineering by UFPE in 1995, in Recife, PE, Brazil; Doctor degree in Aeronautical Engineering by ITA in 2002, in São José dos Campos, SP, Brazil; and Post-Doctor degree in Aeronautical Engineering by ITA in 2009, in São José dos Campos, SP, Brazil.

Actually, he is doing a new post-doctorate curse in Aerospace Engineering at ITA. The last researches are based on thermochemical non-equilibrium reentry simulations in Earth and thermochemical non-equilibrium entry simulations in Mars. They are: Maciel, E. S. G., and Pimenta, A. P., "Thermochemical Non-Equilibrium Reentry Flows in Two-Dimensions – Part I', WSEAS Transactions on Mathematics, Vol. 11, Issue 6, June, pp. 520-545, 2012; Maciel, E. S. G., and Pimenta, A. P., "Thermochemical Non-Equilibrium Entry Flows in Mars in Two-Dimensions – Part I', WSEAS Transactions on Applied and Theoretical Mechanics, Vol. 8, Issue 1, January, pp. 26-54, 2013; and he has three published books, the first one being: Maciel, E. S. G., "Aplicações de Algoritmos Preditor-Corretor e TVD na Solução das Equações de Euler e de Navier-Stokes em Duas Dimensões", Recife, PE, Editor UFPE, 2013. He is interested in the Magnetogasdynamic field with applications to fluid dynamics and in the use of ENO algorithms.